Spring 2015

Investigation of Lanthanide-Doped Anatase TiO2 Core-Shell Nanoparticles For Photocatalysis and Gas Sensing

Rezwanur Rahman

Follow this and additional works at: https://bearworks.missouristate.edu/theses

🔥 Part of the Materials Science and Engineering Commons

INVESTIGATION OF LANTHANIDE-DOPED ANATASE TIO$_2$ CORE-SHELL

NANOPARTICLES FOR PHOTOCATALYSIS AND GAS SENSING

A Masters Thesis

Presented to

The Graduate College of

Missouri State University

In Partial Fulfillment

Of the Requirements for the Degree

Master of Science, Materials Science

By

Rezwanur Rahman

May 2015

INVESTIGATION OF LANTHANIDE-DOPED ANATASE TIO$_2$ CORE-SHELL NANOPARTICLES FOR PHOTOCATALYSIS AND GAS SENSING

Department of Physics Astronomy and Materials Science

Missouri State University, May 2015

Master of Science

Rezwanur Rahman

ABSTRACT

Anatase TiO$_2$ has been shown to be potential applications for photo-remediation of chemical waste as well as for photocatalytic splitting of water. The catalytic properties of TiO$_2$ materials can be modified by doping with lanthanide (Ln) ions. In order to minimize the distortion and/or change of the structure of TiO$_2$ nanoparticles, surface doping of anatase TiO$_2$ nanoparticles ($\sim$ 14 nm) with several Ln ions (Nd^{3+}, Gd^{3+}, Eu^{3+}, Yb^{3+}) has been successfully made. X-ray diffraction (XRD) and Raman characterization shows that the anatase phase of treated nanoparticles is well preserved. Scanning electron microscopy (SEM) shows that the majority of the nanoparticles exhibit nanocrystalline shape and transmission electron microscopy (TEM) shows TiO$_2$ core and Ln-TiO$_2$ shell structure having a uniform phase consistent with the anatase atomic-scale structure. Energy Dispersive X-ray (EDX) spectroscopy confirms the presence of Ln ions within the Ln-TiO$_2$ nanoparticles. Temperature dependent *in situ* optical measurements show an increase in photoluminescence (PL) in forming gas (5% H$_2$ + 95% Ar) at 520 °C which is attributed to nanoparticle modification (i.e. core-shell structure) induced by doping and use of the hydrothermal treatment. The increase in the distinguishable features in the PL spectrum at low and high (near IR) wavelength regions are attributed to various contributions from oxygen-vacancies and trapped electrons, respectively. Furthermore, X-ray Photoelectron Spectroscopy (XPS) has been performed to observe the shift in the local chemical states due to Ln incorporation into the anatase TiO$_2$ structure.

KEYWORDS: nanoparticles, Lanthanides, XRD, TEM, XPS, photocatalysis, PL.

This abstract is approved as to form and content

Robert A Mayanovic, Ph.D.
Chairperson, Advisory Committee
Missouri State University

INVESTIGATION OF LANTHANIDE-DOPED ANATASE TIO$_2$ CORE-SHELL

NANOPARTICLES FOR PHOTOCATALYSIS AND GAS SENSING

By

Rezwanur Rahman

A Masters Thesis
Submitted to the Graduate College
Of Missouri State University
In Partial Fulfillment of the Requirements
For the Degree of Master of Science, Materials Science

May 2015

Approved:

_____
Robert A Mayanovic, Ph.D.

_____
Kartik C Ghosh, Ph.D.

_____
Kathryn M Fichter, Ph.D.

_____
Julie Masterson, Ph.D, Dean, Graduate College

ACKNOWLEDGMENTS

TABLE OF CONTENTS

LIST OF TABLES

LIST OF FIGURES

INTRODUCTION

TiO$_2$ nanostructured materials are being investigated for a number of applications, including photocatalysis, gas sensing, solar cell devices, antibacterial agents, and self-cleaning coatings.[1] Photocatalytic activity as well as other physical and chemical properties of the material is enhanced by the higher surface area to volume ratio inherent in nanostructured materials. Of the common TiO$_2$ phases, anatase is the most photocatalytic, having highly suitable energy band vs NHE potential characteristics.[1] However, anatase TiO$_2$ remains inefficient, absorbing primarily UV light due to its wide bandgap (3.2 eV).[2] Doping with lanthanide (Ln) ions has been found to be advantageous for enhancing the optical and catalytic properties of TiO$_2$ nanoparticles[3] including enhancing the photoreceptivity of visible light.4 However, the incorporation of larger amounts (i.e., greater than doping level) of Ln ions results in substantial disruption of the crystalline phase of anatase TiO$_2$ nanostructures. Hydrothermal Ln-incorporated overgrowth of TiO$_2$ nanoparticles and nanostructures may result in less disruption of the crystalline structure. In this work, we have fabricated TiO$_2$-Ln$_x$Ti$_{1-x}$O$_2$ core-shell nanoparticles (Ln = Nd, Eu, Gd, Yb) using hydrothermal methods. In situ photoluminescence (PL) characterization was made of the NPs under different atmospheres and to high temperatures, from which we can infer about the photocatalytic ability of the samples.[5] Photoluminescence intensity has been found to correspond to photocatalytic ability in indirect bandgap semiconductors. Oxygen vacancies can be

manipulated by atmospheric exposure to oxidizing and reducing gasses, and in this study we observe these changes in situ via photoluminescence.

1.1 Aims and Goals

In 1972, Fujishima and Honda demonstrated photocatalytic splitting of water using a TiO_2 electrode under ultraviolet light. After this development, research began in earnest on TiO_2 to make it an efficient photocatalyst by using various techniques. One of the popular techniques is to dope different types of elements with TiO_2 to attain the desirable characteristics for photocatalysis. The initial goal of the research is to observe the change in physical, structural and optoelectronic behavior of hydrothermally treated rare earth doped TiO_2. The reason for choosing rare earth dopant is the availability of 4f shell of rare earth elements for band gap modification of the typical TiO_2. Typical anatase TiO_2 has a band gap of 3.2 eV which makes it an inefficient photocatalyst under sunlight. Doping of TiO_2 with lanthanide (Ln) metal dopants may alter the photocatalytic properties, potentially expanding responsiveness into the visible spectrum.

1.2 Extent of Research on TiO_2 for Photocatalysis

Photocatalysis research on TiO_2 can be classified based on applications as following:

1. Drinking water purification

2. Waste water treatment

3. Killing of microorganisms and pathogens

4. Destruction of air pollutants/air purification

5. Conversion or recovery of heavy metal ions/precious metal ions

6. Photocatalytic reactor engineering

7. Oil spill remediation

8. Prevention of algal bloom and algal growth

9. Photocatalytic oxidation coupled with other treatment processes

10. Synthesis of visible light active photocatalytic materials

11. Photocatalytic materials for self-cleaning, superhydrophilic, and antibacterial function

12. Coating technology for product developments

13. Photo-functional composite materials

14. Hydrogen production through water splitting

15. Development of visible light sensitizers and composite materials

16. Photocatalytic conversion of N_2/CO_2

17. Nano-structured TiO_2 electrodes for dye-sensitized solar cells

18. Solar reactor design and development

19. Photocatalysis for chemicals synthesis and manufacturing

20. Development of new synthetic method utilizing greener processes and reagents

21. Metal corrosion prevention using a TiO_2 photoanode

22. Photocatalyst coating on metal surface for corrosion prevention

23. Development of alternative lithographic process utilizing photocatalysis

1.3 Structure of TiO₂

Titanium dioxide has three main phases: rutile, anatase, and brookite. It has eight polymorphs, i.e., different structural modifications. Among them three metastable phases can be produced synthetically (monoclinic, tetragonal and orthorombic and five other forms (α-PbO₂-like, baddeleyite-like, cotunnite-like, orthorhombic OI, and cubic phases) at high pressure. The main of source of titania is ilmenite ore. Another source rutile is the next most abundant and contains around 98% titania in the ore. Heating in the
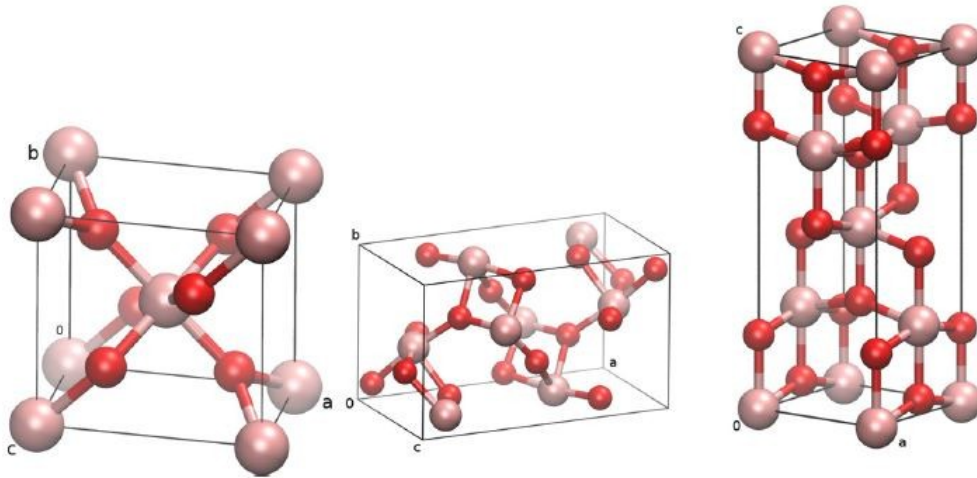
Figure 1. Unit cells of the TiO2 polymorphs: rutile, brookite and anatase (from left to right)

temperature range of 600°-800 °C converts the metastable anatase and brookite phases to the equilibrium rutile phase.

The structure of the three major forms are: rutile (tetragonal), anatase (tetragonal) and brookite (orthorhombic), which can be understood in terms of (TiO_6^{2-}) octahedra differing by the distortion and connectivity of the octahedral chains (Figure 1).[6] The

major structural parameters are summarized in Table. The most stable of these phases is rutile in most temperature and pressure conditions. However, there has been some recent evidence that the anatase phase may be more stable than the rutile phase for very small particle sizes (≤15 nm).[7]

Table 1. Physical properties of bulk TiO2. The space group notation is that of Schöenflies. The point group is the notation of Hermann–Mauguin.[7]

	Anatase	Rutile	Brookite
Crystal System	Tetragonal	Tetragonal	Rhombohedral
Space group	D_{4h}^{19}	D_{4h}^{14}	D_{2h}^{15}
Point group	I4$_1$/amd	P4$_2$/mnm	Pbca
a (Å)	3.782	4.584	5.436
b (Å)	3.782	4.584	9.116
c (Å)	9.502	2.953	5.135
ρ (g/cm)	3.8-3.9	4.2-4.3	3.9-4.1

1.4 TiO$_2$ as a Photocatalyst

Titanium dioxide generates a pair of a conduction band (CB) electron and a Valence Band (VB) hole in the solid oxide lattice upon absorbing a photon with energy greater than 3.2 eV (or wavelength<388 nm). The subsequent charge transfers at the

interface initiate various types of redox reactions under the ambient condition (in both air and water). Any semiconductor with an appropriate magnitude of the bandgap and the position of band edges is able to initiate photoinduced redox reactions on its surface.
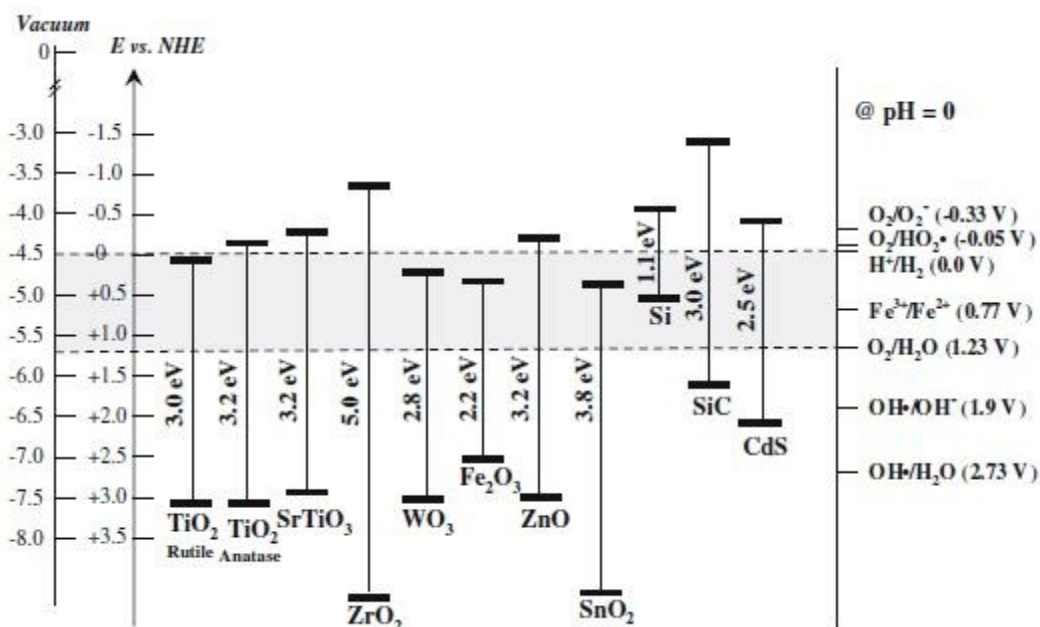
Figure 2. Energy-level diagram showing the conduction band and valence band edge positions of various semiconductors at pH 0 along with selected redox potentials. The energy scales are referenced against both the vacuum level and the normal hydrogen electrode (NHE).[1]

Figure 2 compares the bandgap and the band edge position of various semiconductors at pH = 0. Other wide bandgap semiconductors with high positive values of E_{vb} such as ZnO, WO$_3$, and SnO$_2$ often show some oxidative photocatalytic reactivities. However, in most cases their photoactivities are lower than those of TiO$_2$. The strong remedial power of TiO$_2$ photocatalysts is mainly ascribed to the strong oxidation potential of VB holes (E_{vb}=+2.7 V NHE at pH 7) or OH radicals that are

produced on the TiO_2 surface through the reaction of VB holes with the surface hydroxyl groups or adsorbed water molecules. The reaction of a VB hole should accompany the CB electron transfer to maintain the electro neutrality of the catalyst particle and the typical scavenger of CB electrons is O_2. Such a sensitized photooxidation in the TiO_2-mediated remediation is closely compared with the nature's photochemical cleanup mechanisms.[1]

1.5 Rutile versus Anatase for Photocatalysis

The anatase is more suitable than the rutile TiO_2 for photo-catalysis because the former has a smaller indirect band gap whereas the latter has a direct band gap as the primary band gap or its indirect band gap is very similar to its direct band gap. Indirect band gap semiconductors generally exhibit longer charge carrier life times compared to direct gap materials. A shorter electron-hole pair life in rutile than in anatase would make it less likely for charge carriers to participate in surface reactions. Transient photoconductivity measurements on single crystalline samples show longer charge carrier lifetimes in anatase than in rutile phase.[8]

Surface properties play an important role in charge transfer and adsorption of molecules. The surface properties may differ largely for the same material for different surface orientations or reconstructions and consequently may contribute to the observation of pronounced surface effects in photocatalytic activities. Surface properties can be subdivided into (i) chemical effects: coordination structure of surfaces that controls adsorption of molecules, (ii) electronic structure of the clean surface or defects

and adsorbate (e.g. hydroxyl)-induced states that may be crucial for charge trapping and separation at the surface, (iii) interaction of molecules with surface defects, and (iv) surface potential differences (such as work function differences measured in vacuum or flat band potentials in aqueous solution) may affect charge transfer from the photocatalyst to molecules. The relative position of the conduction band minimum (CBM) in rutile and anatase is still controversial. The large band gap of anatase suggests the CBM in anatase to be higher than for rutile. However, recent results are suggesting that conduction band of anatase is actually lower than that of rutile.[8]

1.6 Gas Sensing:

Hydrogen is one of the powerful clean energy carriers. It is the ultimate fossil fuel candidate. It has a high heat of combustion (142 kJ/g), a low minimum ignition energy (0.017 mJ), a wide flammable range (4–75%), and a high burning velocity. The combustion product of hydrogen is water. That's why it is free from contamination and can be converted into hydrogen and oxygen again for cyclic duty. Liquid hydrogen has been used for rocket fuels. Hydrogen is highly used in semiconductor processing, petroleum extraction, metal smelting, glassmaking, and in the chemical industry because of its strong reducing properties. Hydrogen can also be applied in environmental protection, seismic surveillance area such as for indicating certain type of bacterial infection, biomedical hazard, or detection of environmental pollution.[9]

Hydrogen gas is odorless, tasteless and colorless. It cannot be detected by humans without using a detection device. The wide flammable range and low ignition energy

8

makes it easy inflammable and explosive. Therefore accurate and quick hydrogen detection is necessary during the production, storage and use of hydrogen. It is also essential for controlling the hydrogen concentration of semiconductor manufacturing, nuclear reactors, and coal mines etc.

As the traditional hydrogen detectors such as mass spectrometers, gas chromatographs and specific ionization gas pressure sensors are limited by their expensive cost, large size, slow response, high temperature of use, and potential safety hazards. Cheap hydrogen gas sensors of smaller size, and low power consumption, as well as lower operation temperature and faster response are required for widespread use such as portable and in-situ monitoring. The rapid development of the hydrogen economy has promoted research on new types of hydrogen gas sensors with accurate hydrogen sensing, near room temperature (RT) operation without power sources and compatibility with microelectronic integrated circuits.[9]

There are many types of the commercially available hydrogen sensors. These include optical and acoustic electrochemical, semiconductor, thermoelectric, or metallic ones. However, semiconductor sensors exhibit fast response, long-term stability high sensitivity and potential for integration in hydrogen sensing performance than the other types. Still these kind of hydrogen sensors suffer from high operational temperatures, which requires high power consumption. They also have potential safety hazards. Again, the cross selectivity to other combustible or reducing gases is another critical issue, which should be restricted to enhance the sensing accuracy. Currently, semiconductor nanostructures such as thin films and nanowires have been employed as sensing materials

for building high-performance hydrogen sensors due to their high specific surface area and novel electron transportation properties. For example, mesoporous thin films or nanotube arrays synthesized by anodic oxidization show enhanced hydrogen sensing properties compared to traditional film-based sensors due to the greater specific surface area. 1D nanostructures show much higher sensing performance such a broader limit of detection (LOD), lower operation temperature, higher sensitivity and response time than thin films. Nanoparticles-decorated semiconductor nanostructures have also been widely investigated for increasing of sensitivity and selectivity to hydrogen gas.[9]

1.7 Lanthanide (Ln) Doping:

Doping is a technique that can be used to vary the number of electrons and holes in materials. Energy transfer via photon and/or assisted phonon transitions may easily take place in a Ln-doped TiO_2 material since Ln ions lend easily accessible energy levels such as $^5D_1 \rightarrow {}^7F_1$, $^5D_0 \rightarrow {}^7F_j$ (j = 1, 2, 3, 4) transitions of Eu^{3+} ions will cause visible luminescence peaking at 543, 598, 620, 665, and 694nm.[10] In addition, Ln-doped TiO_2 have the capacity to enhance photocatalytic activity of a TiO_2 nanomaterial due to following properties: ; (i) unique textural properties (mesoporosity with larger BET surface areas and pore sizes); (ii) quantum size effect; (iii) interesting surface compositions (more hydroxyl oxygens, adsorbed oxygen and some percentage of Ti^{3+} species at the surface of the products with respect to pure TiO_2). The increase in photoactivity is probably due to red shifts to a longer wavelength, the higher adsorption, and the increase in the interfacial electron transfer rate. Nevertheless, there are two major

controversies: i) whether the lifetime of transition metal or Ln ions-doped TiO_2 semiconductor nanoparticles can be shortened by orders of magnitude caused by quantum size effects; ii) lanthanide ions incorporate into the lattice sites of the host or be adsorbed on the surface because of the different radius and valence between Ln ions and cationic of host.[3] The mathematical study on Ln doping shows 4f electron levels are found to occupy the bottom of the CB together with Ti 3d states, which supposes a negligible decrease of the band gap.[11]

The ground state electron configurations of the lanthanides of this study are:

Nd: [Xe] $6s^2$ $4f^4$

Eu: [Xe] $6s^2$ $4f^7$

Gd: [Xe] $6s^2$ $4f^7$ $5d^1$

Yb: [Xe] $6s^2$ $4f^{14}$

1.8 Role of Oxygen Vacancy in TiO2 for Photocatalysis and Gas Sensing:

Oxygen vacancies play an important role on the photocatalytic and gas sensing properties of Ln-doped TiO_2 NPs. Density Functional Theory (DFT) based calculations reveal the effect of lanthanide doping in TiO_2, which provides persuasive evidence that the notable catalytic properties of these systems arise from the facilitated oxygen vacancy.[11,12] It has been reported that titania can be reduced by annealing in an oxygen poor atmosphere. The reduction of TiO_2 takes place through an increase in the amount of oxygen vacancy under mild thermal treatments. Ti^{4+} cations are reduced and migrate to interstitial positions, further reducing neighboring cations under hard thermal treatment.

In any case, vacancy formation is more likely to occur in soft synthesis methods.It is generally involved in the catalytic activity of TiO_2 through O atom donation or uptake in oxidation and reduction reactions.[11]

EXPERIMENTAL AND CHARACTERIZATION TECHNIQUES

2.1 Hydrothermal Processing:

Hydrothermal synthesis is a process that utilizes single or heterogeneous phase reactions in aqueous media at elevated temperature ($T>25$ºC) and pressure ($P>100$ kPa) to crystallize ceramic materials directly from solution. Syntheses are typically conducted at self-assisted pressure, which corresponds to the saturated vapor pressure of the solution at the specified temperature and composition of the hydrothermal solution. Upper limits of hydrothermal synthesis prolong to over 1000ºC and 500 MPa pressure. Hydrothermal crystallization processes afford excellent control of morphology (fibrous, spherical, cubic, and plate-like) size (from a couple of nanometers to less than a micron), and degree of agglomeration. These characteristics can be controlled in wide ranges by varying reaction temperature, pressure and concentrations of the reactants or stirring speed.[13]

2.2 SEM, TEM AND EDX:

The scanning electron microscope (SEM) is one of the most multipurpose instruments available for the investigation and analysis of the microstructure morphology and chemical composition characterizations. The SEM utilizes a focused electron beam to scan across the surface of the specimen systematically, producing large numbers of signals. These electron signals are eventually converted to a visual signal displayed on a cathode ray tube (CRT). Image formation in the SEM is dependent on the acquisition of

signals produced from the electron beam and specimen interactions. The limit of resolution is defined as the minimum distances by which two structures can be separated and still appear as two distinct objects. Resolution in a perfect optical system can be described mathematically by Abbe's equation[14] as follows:

$d = 0.612\, l\,/n\, \sin\alpha$

where, d = resolution, l = wavelength of imaging radiation, n = index of refraction of medium between point source and lens, relative to free space, and α = half the angle of the cone of light from specimen plane accepted by the objective (half aperture angle in radians); $n\sin\alpha$ is often called numerical aperture (NA).

To obtain a good image we need to control the instrumental parameters (accelerating voltage, working distance etc.). We need to set the accelerating voltage correctly for proper imaging of the sample. If the accelerating voltage is too high then it could affect the base plate and we will get wrong information about the sample whereas there will be shadow effects if the voltage is too low. Working distance must be maintained according to the accelerating voltage. The image could be blurred if the working distance is large. On the other hand low working distance could produce a darker image. The working chamber has to be at a high vacuum in order to avoid the collision among the electrons and other gases. If the chamber is not at high enough vacuum, we will not be able to get an image of the sample. We also need to control the aperture. Low aperture size is necessary for beam-sensitive samples. For most of the applications, optimum aperture size should be kept. High aperture size is only required for analytical purposes.[14]

Transmission electron microscopy (TEM) is an imaging technique where a beam of electrons is focused onto a specimen causing an enlarged version to appear on a fluorescent screen or layer of photographic film. In TEM a thin specimen is illuminated with primary electrons. The images can be formed in TEM by using either the central spot or the scattered electrons. The electrons that are used to form the image are selected by insertion of the electron beam through an aperture into the back focal plane of the objective lens. Most of the diffraction pattern is blocked so that only a fraction of the electrons are made visible through the aperture. External drives are used to control the aperture so that either the direct electrons or scattered electrons go through it. If the direct beam is selected, then the resultant image is known as a bright-field image. On the other hand, if scattered electrons of any form are selected then it's called a dark-field image.[15]

Energy-dispersive X-ray spectroscopy (EDS or EDX) is an analytical technique used for the elemental analysis or chemical characterization of a sample. When electrons of appropriate energy impinge on a sample, they cause the emission of x-rays whose energies and relative abundance depend upon the composition of the sample. Using this measure to analyze the elemental content of micro-volumes is what we commonly mean by microanalysis. Microanalysis is the easiest method for analyzing microscopic samples. It is sensitive to low concentrations—minimum detection limits (MDL) are below 0.1% in the best cases and typically less than 1%; and its dynamic range runs from the MDL to 100%, with a relative precision of 1% to 5% throughout the range. Furthermore, the technique is practically nondestructive in most cases, and requirements for sample preparation are minimal.[16]

15

2.3 X-ray diffraction (XRD):

Powder X-ray diffraction offers a convenient method to characterize materials by using their constituent crystal structures. A crystalline sample contains regular repeating arrays of atoms. When the sample is irradiated by a monochromatic X-ray beam, it generates a unique spectrum in the form of diffraction peaks as a function of scattering angle. A powder diffractogram is used to identify crystalline components of a sample by the diffraction process. Powder diffraction can easily and unambiguously identify the crystalline forms of a material. XRD can quantify phase amounts, solve crystal structures, and refine crystal structures, determine micro-structural characteristics such as crystallite size, shape and strain, identify the spatial distribution of phases down to the micron level using mapping microdiffraction, and investigate phase stability and reactions under a range of different conditions e.g. time, temperature, pressure and atmosphere.[17]

2.4 Raman Spectroscopy:

In Raman spectroscopy, the sample is irradiated by intense laser beams in the UV-visible region. The scattered light is generally observed in the direction perpendicular to the incident beam (υ_0). The scattered light consists of two types: one, called Rayleigh scattering, which is strong and has the same frequency as the incident beam, and the other, called Raman scattering, which is very weak ($\sim 10^{-5}$ of the incident beam) and has frequencies $\upsilon_0 \pm \upsilon_m$, where υ_m is a vibrational frequency of a molecule. The $\upsilon_0\text{-}\upsilon_m$ and $\upsilon_0+\upsilon_m$ lines are called the Stokes and anti-Stokes lines, respectively (Figure 3).[18] Thus, in Raman spectroscopy, we measure the vibrational frequency (υ_m) as a shift from the

incident beam frequency (υ_0). Raman spectra are measured in the UV-visible region where the excitation as well as Raman lines appear.[18]

Rayleigh

Stokes

anti-Stokes

−459

−314

−218

+218

+314

+459

Intensity

0

Raman shift (cm^{-1})
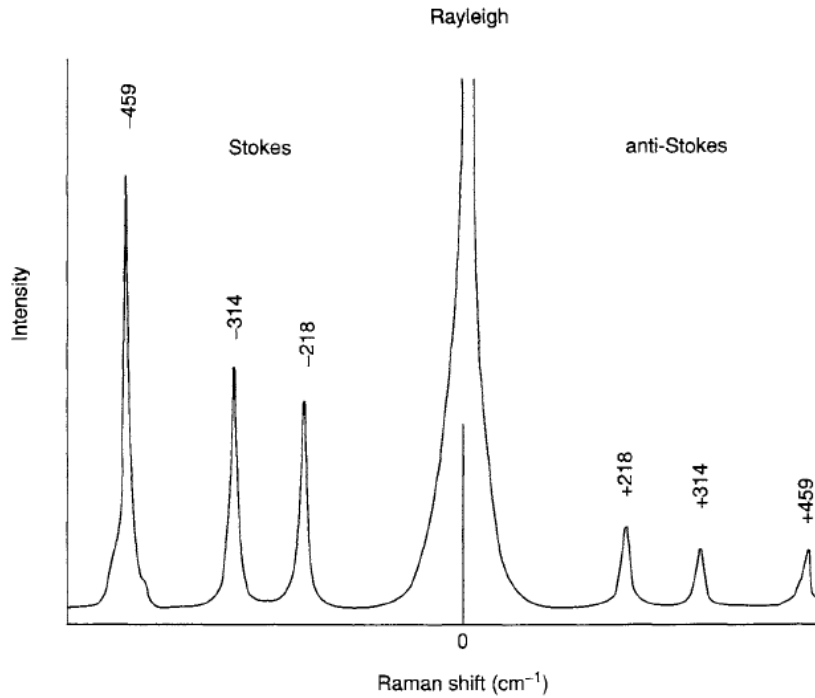
Figure 3. Raman spectrum of CCl$_4$ (488.0 nm excitation)

2.5 Photoluminescence (PL):

Photons are absorbed and electronic excitations are created when light of sufficient energy is incident on a material. After a while, these excitations relax and the electrons return to the ground state. PL occurs due to the radiative relaxation of electronic excitations. Information about the photoexcited material can be found by analyzing PL. The PL spectrum can provide information about the transition energies associated with the electronic excitations. Transition energies can be used to determine electronic energy

levels of a material. The relative rates of radiative and nonradiative recombination can be measured by PL. Information about the electronic states and bands can be found by observing the variation of PL intensity with external parameters like temperature and applied voltage. PL analysis is a useful tool in the characterization of surfaces. The energy distribution and density of interface states can be ascertained by studying the excitation intensity dependence of the PL spectrum. The presence of surface adsorbates affects the intensity of the PL signal. The depth of the trap can be determined by observing thermal activation in temperature-dependent PL. PL can be used to study virtually any surface in any environment; that is why it can be used to monitor changes induced by surface modification in real time. PL is usually not sensitive to the sample chamber pressure. Henceforth, it can be used to study surface properties in relatively high-pressure semiconductor growth reactors. Although PL depends quite strongly on temperature, with liquid helium temperatures being required for the highest spectral resolution, whereas room-temperature measurements are sufficient for many purposes. In addition, PL has little effect on the surface under investigation. Low excitation can minimize sample heating and photoinduced changes. In situ PL measurements require optical access to the sample chamber. Compared with other optical methods, PL is less rigorous about sample thickness, beam alignment, and surface flatness. The advantages of PL analysis listed above derive from the power to probe fundamental electronic properties and the simplicity of optical measurements. The fundamental disadvantage of PL analysis also follows from the reliance on optical techniques: the sample under investigation must emit light. Indirect-bandgap semiconductors, where the conduction

band minimum is separated from the valence band maximum in momentum space, have

inherently low PL efficiency. Nonradiative recombination tends to dominate the

relaxation of excited populations in these materials. This problem can be augmented by

poor surface quality, where rapid nonradiative events may occur. Nevertheless, once a PL

signal is detected, it can be used to characterize both nonradiative and radiative

mechanisms. Although it may not be possible to identify directly the nonradiative traps

via PL, their signature is evident in several types of PL measurements. Another

shortcoming of PL is the difficulty in estimating the density of interface and impurity

states. When these states have radiative levels, they are readily identified in the PL

spectrum, and the size of the associated PL peaks provides a relative measure of their

presence in the sample. However, measuring the absolute density of these states is a far

more formidable task and typically requires an exhaustive analysis of the excitation

intensity dependence of the PL signal.[19]

2.6 X-ray photoelectron spectroscopy (XPS):

X-ray photoelectron spectroscopy (XPS) owes its quantification aspect to

Einstein's explanation of the photoelectric effect in 1905. XPS has excitation energies

above a few hundred eV to the hard X-ray regime. Therefore, both valence levels and

core levels are readily observable in XPS spectra. The fundamental energy conservation

equation in photoemission is the following:

$$h\upsilon = E_{Vacuum\ binding} + E_{kinetic} + V_{charge} + V_{bias}$$

$$= E_{Fermi\ binding} + \phi_{spectrometer} + E_{kinetic(2)} + V_{charge} + V_{bias}$$

in which h is Planck's constant; υ is the photon frequency; $E_{Vacuum\ binding}$ is the binding energy of a given electron relative to the vacuum level of the sample; $E_{kinetic}$ is the kinetic energy of the emitted electron just as it leaves the sample; $E_{kinetic(2)}$ is the kinetic energy as measured finally in the spectrometer, which may be different from $E_{kinetic}$ by a small contact potential difference if the sample is a solid; $E_{Fermi\ binding}$ is the binding energy relative to the Fermi level or electron chemical potential; $\phi_{spectrometer}$ is the work function of the spectrometer used to measure kinetic energy, V_{charge} is a possible charging potential on the sample which could be built up if the secondary electron and emitted photoelectron current is not fully compensated by flow from the sample ground, V_{bias} is a time-dependent bias potential that may be placed between the spectrometer and the sample.[20] A number of useful effects can be extracted from XPS energy distribution curves: (i) core-level satellites and final-state configuration interaction; (ii) core-level chemical shifts; (iii) core-level multiplet splittings; (iv) core-level vibrational fine structure; (v) photoelectron diffraction and holography; (vi) circular and linear dichroism; (vii) resonant photoemission.[20]

EXPERIMENTAL

3.1 Sample Preparation:

TiO$_2$ nanoparticles were hydrothermally treated to cause surface doping and core-shell particle formation with Nd^{3+}, Gd^{3+}, Eu^{3+}, Yb^{3+} ions. Lanthanide metal salts (NdCl$_3$.6H$_2$O, GdCl$_3$·6H$_2$O, Eu(NO$_3$)$_3$,YbCl$_3$.6H$_2$O) (0.02M) were dissolved in deoxygenated HPLC water, and TiO$_2$ nanoparticles were added to the solutions. About 0.06-0.08 g of high purity (99%) TiO$_2$ anatase nanoparticles were added per 10mL 0.02M of the solution. The pH of the solutions was maintained at ~6 at room temperature by adding either NH$_4$OH or dilute HCl , in order to retain the anatase phase of the nanoparticles. The samples were heated in our Hastelloy C-276 hydrothermal reactor7 for approximately 18 hours above 200°C, and were removed with deionized water.

Figure 4. The hydrothermal reactor and gaskets. On the left is the hydrothermal reactor. The reactor is made of Hastelloy C-276 alloy. On the right, the two gaskets used for sealing between the reactor and lid.

Suspended particles were settled by centrifuge, excess water was decanted, and nanoparticles were evaporated in ambient conditions.

3.2 Calcination:

The nanoparticle samples were calcined at 500°C in air (figure 5), in order to remove hydrocarbons from the surface. The precipitation of Ln cations on TiO_2 NPs can create certain amount of defects which act as recombination centers that decrease the photocatalytic activity. This adverse effect can be mitigated by calcination of the doped TiO_2 NPs.
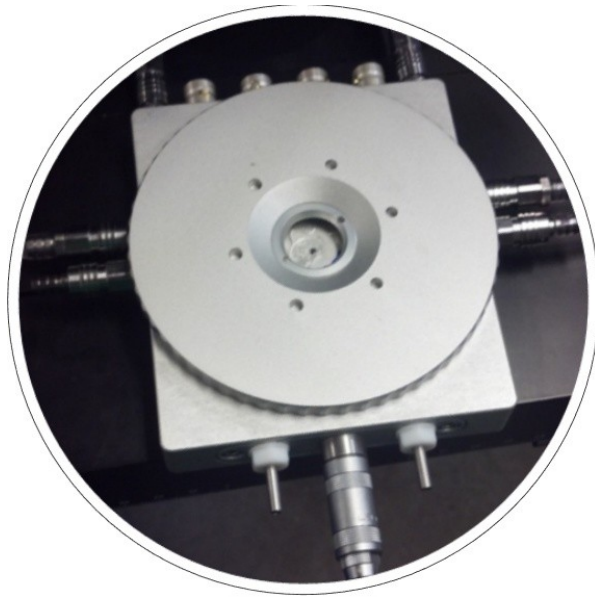
Figure 5. Calcination chamber for the nanoparticles

3.3 XRD:

Powder x ray diffraction (XRD) measurements were performed on each of the samples using a Bruker D8 Discover instrument (Figure 6). The XRD instrument was operated at 40 kV and 40 mA with characteristic x-ray radiation from a Cu tube (Cu Kα with $\lambda = 1.54184$ Å). Reitveld refinement analyses were made of XRD spectra averaged from 6 individual spectra. XRD data were analyzed by using DIFFRAC plus Topas software.

Figure 6. Bruker D8 Discover instrument

The radius of the individual spherical nanocrystals has been estimated using the Scherrer equation

$$\tau = \frac{K\lambda}{\beta\cos\theta}$$

Where, K is a shape factor constant, λ is the x-ray wavelength, β is the full width half maximum (FWHM) of a broadened diffraction peak, and θ is the angle that the diffraction peak was detected at.[7]

3.4 SEM, TEM and EDX:

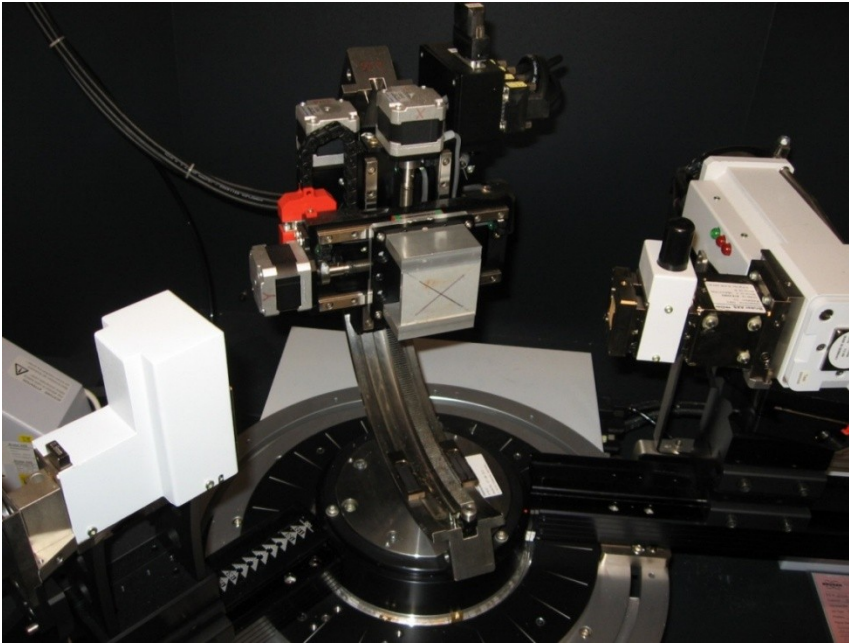Scanning electron microscopy (SEM) and energy-dispersive x-ray spectroscopy (EDX) using an FEI Quanta 200 instrument (figure 7), operating at 2~20 kV, were performed on each of the samples of this study and on the TiO_2 NPs. The SEM-EDX spectroscopy was made using a Field Emission Gun (FEG). The samples were imaged on carbon-backed tape. Transmission electron microscopy (TEM) was performed at 300 kV using an FEI Titan HRTEM. Nanoparticle samples were dispersed into heptane solution by using sonication method. Then TEM grids were put into the solution for few seconds to prepare the TEM samples. EDX measurements were performed to determine the elemental quantification by using both SEM and TEM systems.

3.5 Raman and PL:

In-situ measurements were performed using a Linkam THMS600 heating stage, in both air and forming gas (5% hydrogen with 95% argon). Samples were heated up to 520°C, on glass slides and aluminum plates, and kept at temperature for 2 hours. During the measurement in forming gas, the gas flow rate was kept at 1.3 LPM. Raman

Figure 7. FEI Quanta 200 instrument of PAMS, Missouri State University

measurements were performed using a solid-state 785 nm laser and a 50X objective. PL

spectra were collected using a 325 nm laser excitation source. Raman spectra were

measured at 25° and 520°C. Room temperature PL intensity is considerably lower at low

temperature than that of higher temperature measurement. To obtain optimum signal, it is

necessary to focus correctly. The focusing was done by using 15× NUV lens The PL data

has been analyzed from fitted curve by using OriginPro 8.5.1software. NGSLabSpec

software has been used to find the peak positions in Raman data.
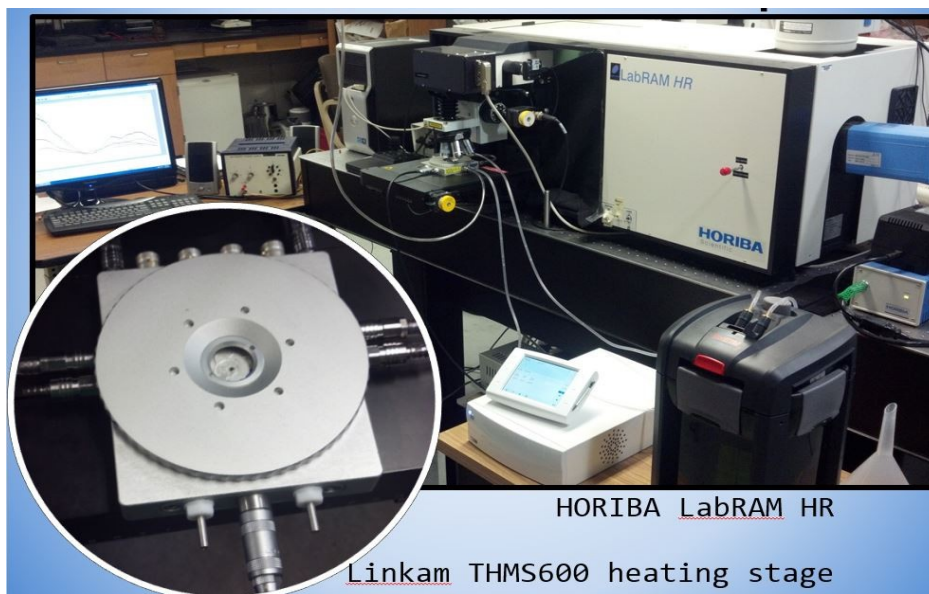
Figure 8. Linkam stage with the Raman setup for In-situ Raman and PL measurement.

3.6 XPS:

XPS was performed in the Jordan Valley Innovation Center (JVIC).
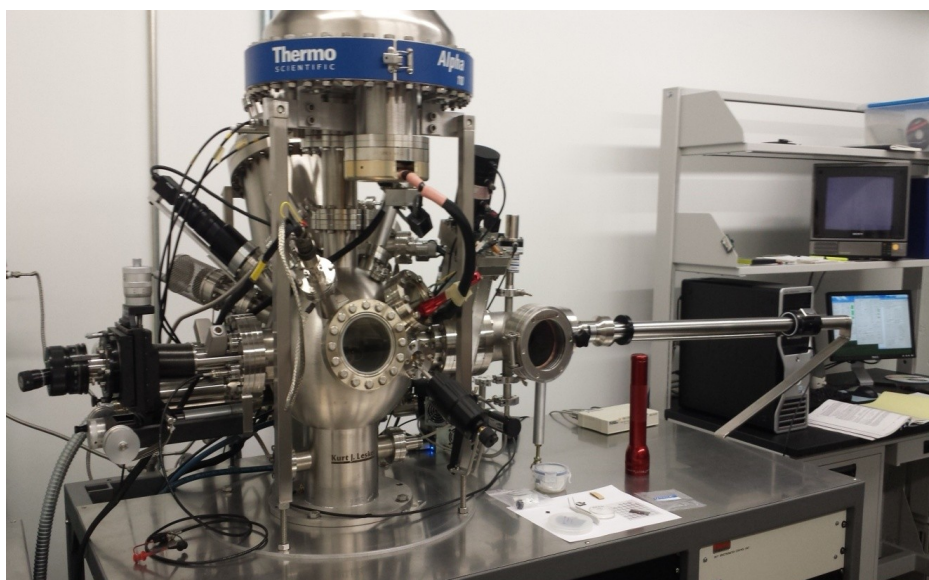
Figure 9. XPS setup in Jordan Valley Innovation Center (JVIC)

The XPS spectrometer uses the characteristic Al-K$_\alpha$ transition at an energy of 1.486 keV or 8.33 Å, which is usually considered to be in the soft X-ray range. Peak identification and chemical compositional analysis were done using the Thermo Advantage chemical analysis software. Fitting of XPS spectra was made using OriginPro 8.5.1 software.

4.1 XRD:

Analysis of x-ray diffraction (XRD) data confirm the preservation of the anatase structure of TiO_2-$Ln_xTi_{(1-x)}O_2$ (Ln-TiO_2) core-shell NPs (Figure 10). This is consistent
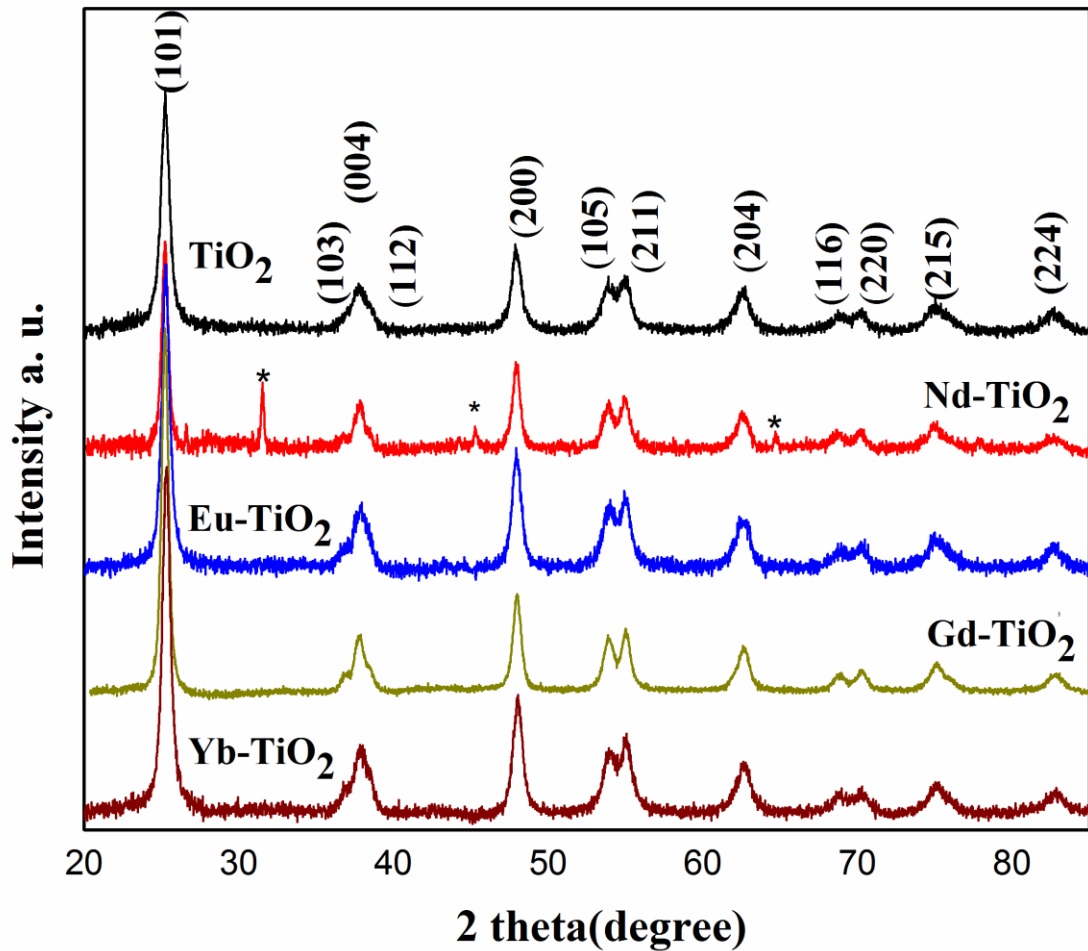
Figure 10. XRD data (a) of Anatase TiO_2 (black), Nd-doped TiO_2 (red), Eu-doped TiO_2 (blue), Gd-doped TiO_2 (dark yellow) and Yb-doped TiO_2 (wine).The XRD data indicate the preservation of anatase structure after the doping. * means contamination peak.

with a small amount of overgrowth, Ln precipitation on and core-shell formation of the

TiO$_2$ NPs. The crystallite size for pure anatase TiO$_2$ is 13.7 nm. Scherrer equation

analysis is consistent with a growth in size of the nanoparticles of 1 to 3nm. This suggests

that the Ln dopants are precipitated within the surface and near-surface regions of the

nanoparticles.
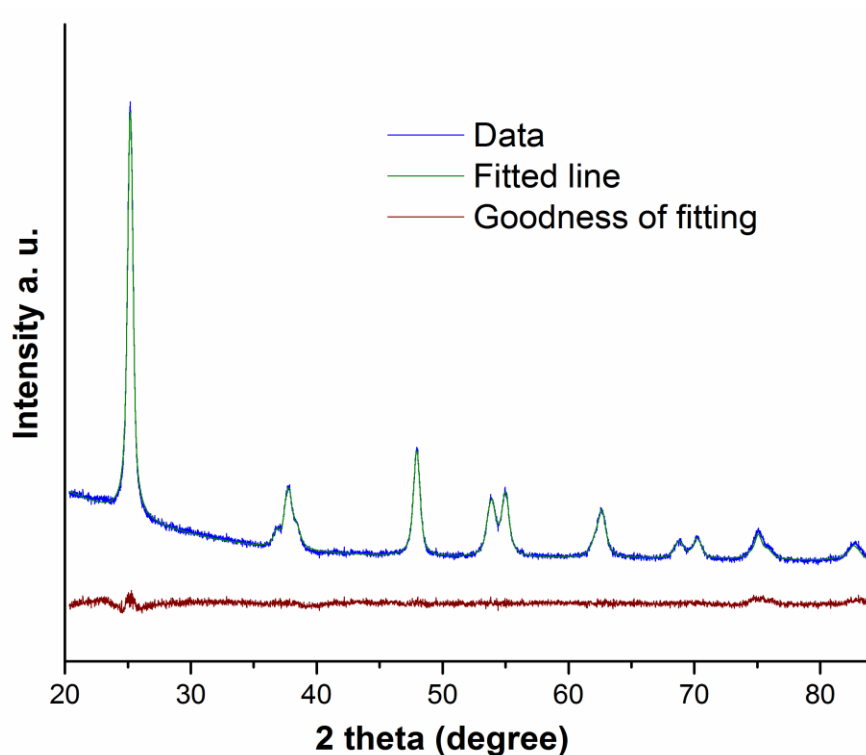
Figure 11. The Rietveld refinement (R$_{wp}$=4.3%) for the representative Gd-TiO2 sample.

The Rietveld refinement analyses from TOPAS software indicate the

lattice parameters and structural information of all the nanoparticle samples. Figure 11

shows one of the representative system (Gd-TiO2 sample). The structural data obtained

from the Rietveld refinement are presented in Table 2.

Table 2. Rietveld refinement analysis data for all the samples

| Sample ID	a (Å)	c (Å)	Crystal Size (nm)
TiO_2	3.8	9.535	13.7
$Yb\text{-}TiO_2$	3.781	9.509	13.27
$Eu\text{-}TiO_2$	3.792	9.507	13.68
$Gd\text{-}TiO_2$	3.783	9.497	16
$Nd\text{-}TiO_2$	3.788	9.501	15.1
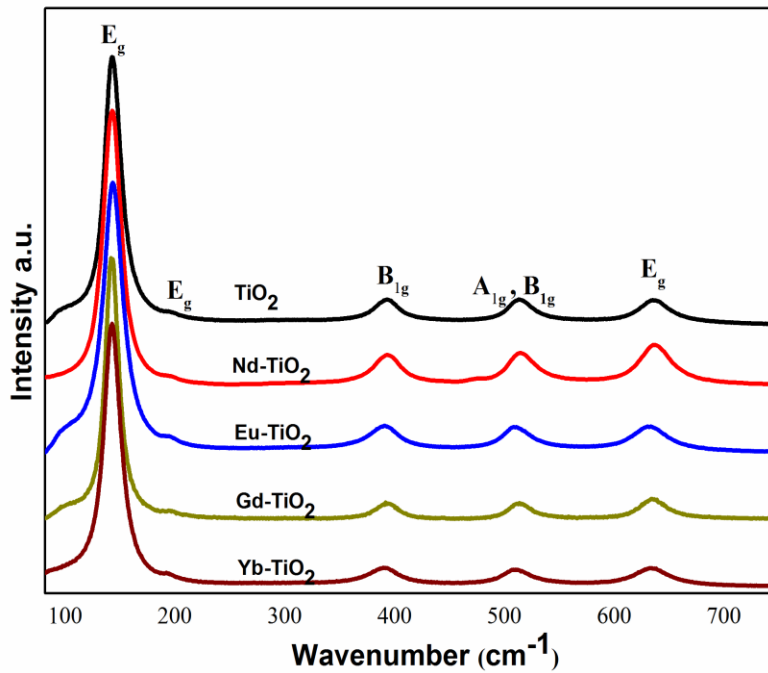
Figure 12. Raman data (a) of Anatase TiO_2 (black), Nd-doped TiO_2 (red), Eu-doped TiO_2 (blue), Gd-doped TiO_2 (dark yellow) and Yb-doped TiO_2 (wine).The data indicate the preservation of anatase structure.
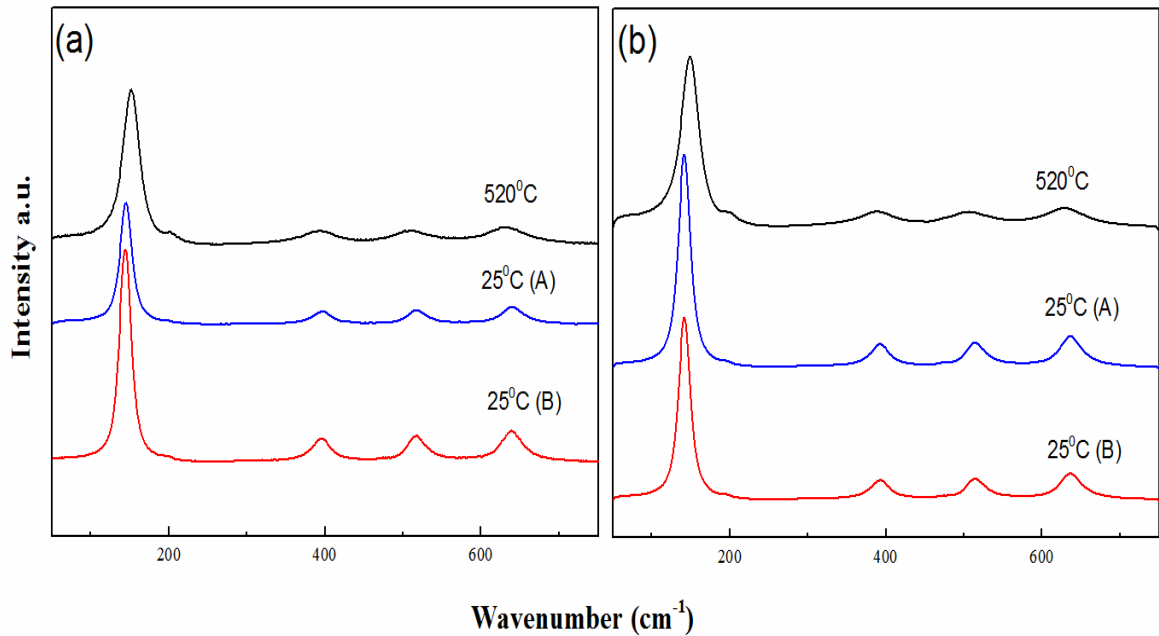
Figure 13. Raman data of (a) Gd-doped TiO_2, (b) Nd-doped TiO_2 measured in air.

4.2 Raman Spectroscopy:

Raman spectra at room temperature show the TiO_2 anatase phase for all the samples. The major peaks were found at $143(E_g)$, $196(E_g)$, $393(B_{1g})$, $515 (A_{1g})$, $519 (B_{1g})$ (superimposed with 515 peak) and $637 cm^{-1}$ (E_g) at room temperature (Figure-12).

Raman spectra collected at 520°C in air show 4-9 cm^{-1} shift (Figure-13) in first peak with compared to the room temperature measurement. This phenomenon has been previously reported by D.Wang et al, which is due to greater thermal expansion and anharmonic coupling at higher temperature.[21] The anatase structure was preserved at 520°C in both air and forming gas.

4.3 SEM, EDX and TEM:

Figures 14 to 17 show the SEM and TEM images and EDX spectra from various nanoparticle samples.
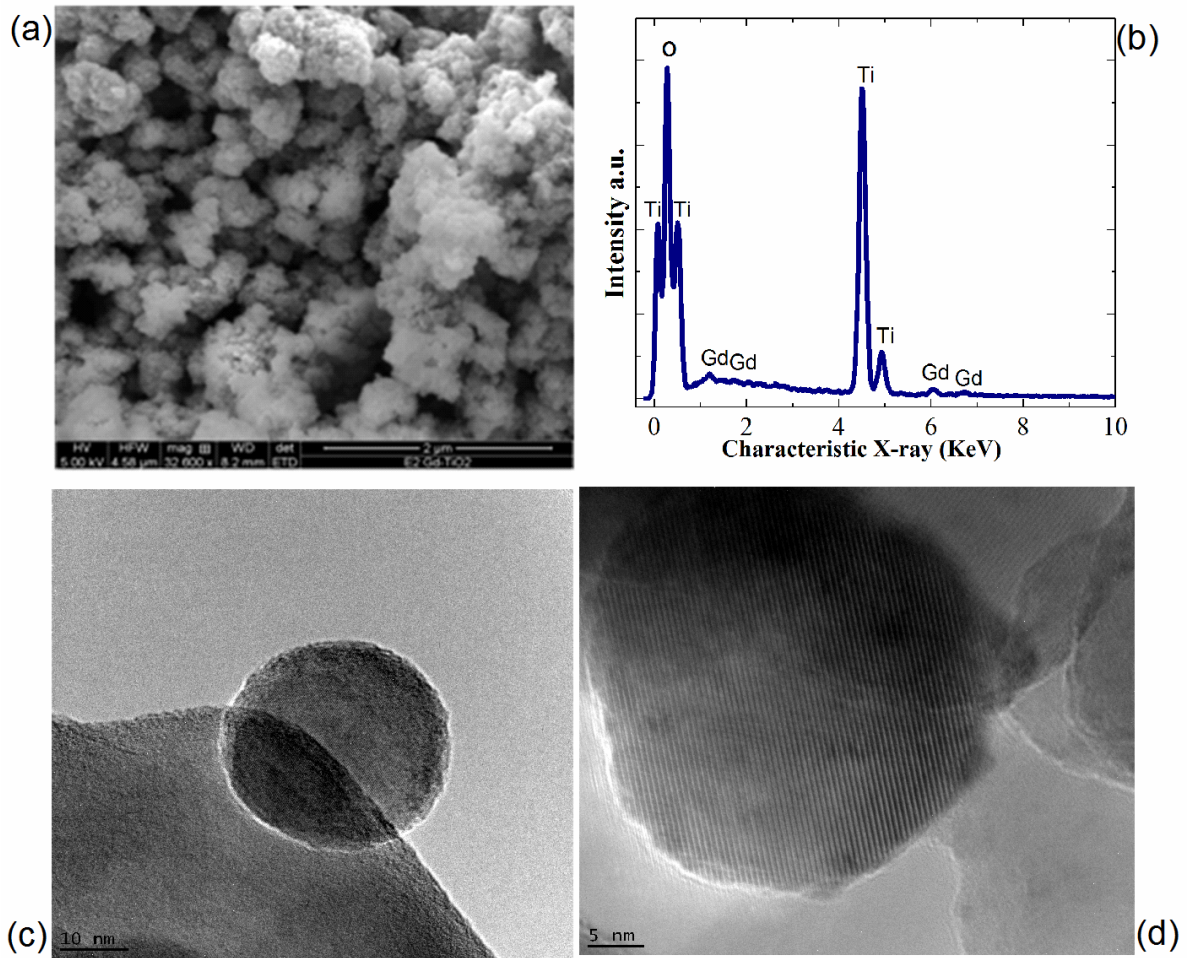
Figure 14. SEM image (Magnification: 32600, at 5KV) (a); EDX data collected from the sample (b), TEM image (10nm scale) (c) and TEM image (5nm scale) (d) of a Gd-TiO$_2$ NP.
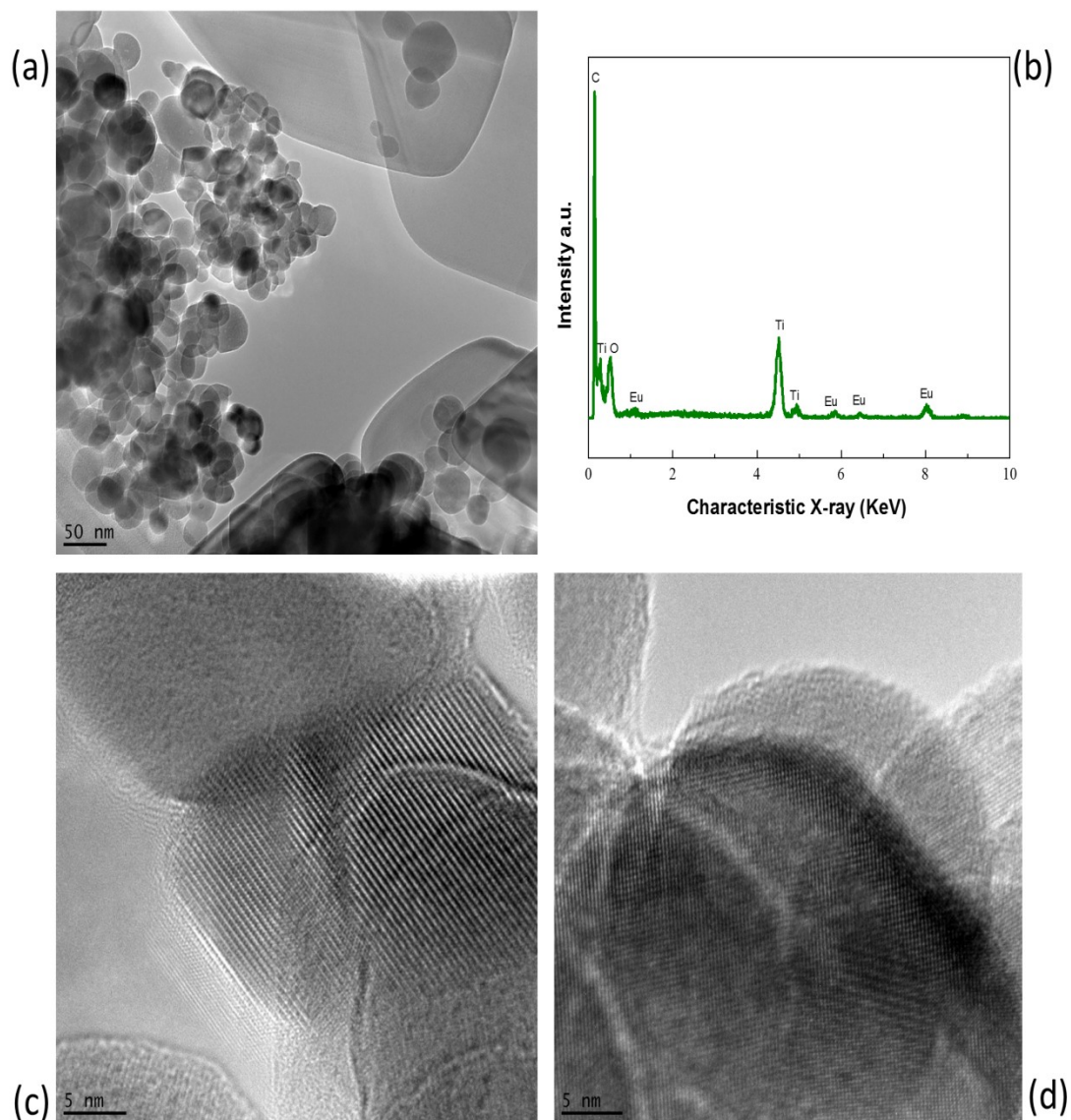
Figure 15. TEM image (50nm scale) (a); EDX data;(b), HRTEM image (5nm scale) (c) and HRTEM image (5nm scale) (d) of Eu-TiO2 NPs.

The EDX analysis confirms the presence of the Ln on the TiO_2 NPs. Furthermore, SEM images reveal an overall morphology (i.e. nanocrystalline nature) and the TEM images confirm the anatase structure of our Ln surface-doped TiO_2 NPs. Many of the nanoparticles exhibit faceting characteristic of the anatase (tetragonal) structure. No

significant change is seen before and after Ln-induced hydrothermal treatment of the

TiO_2 NPs. SEM pictures indicate substantial agglomeration of the anatase
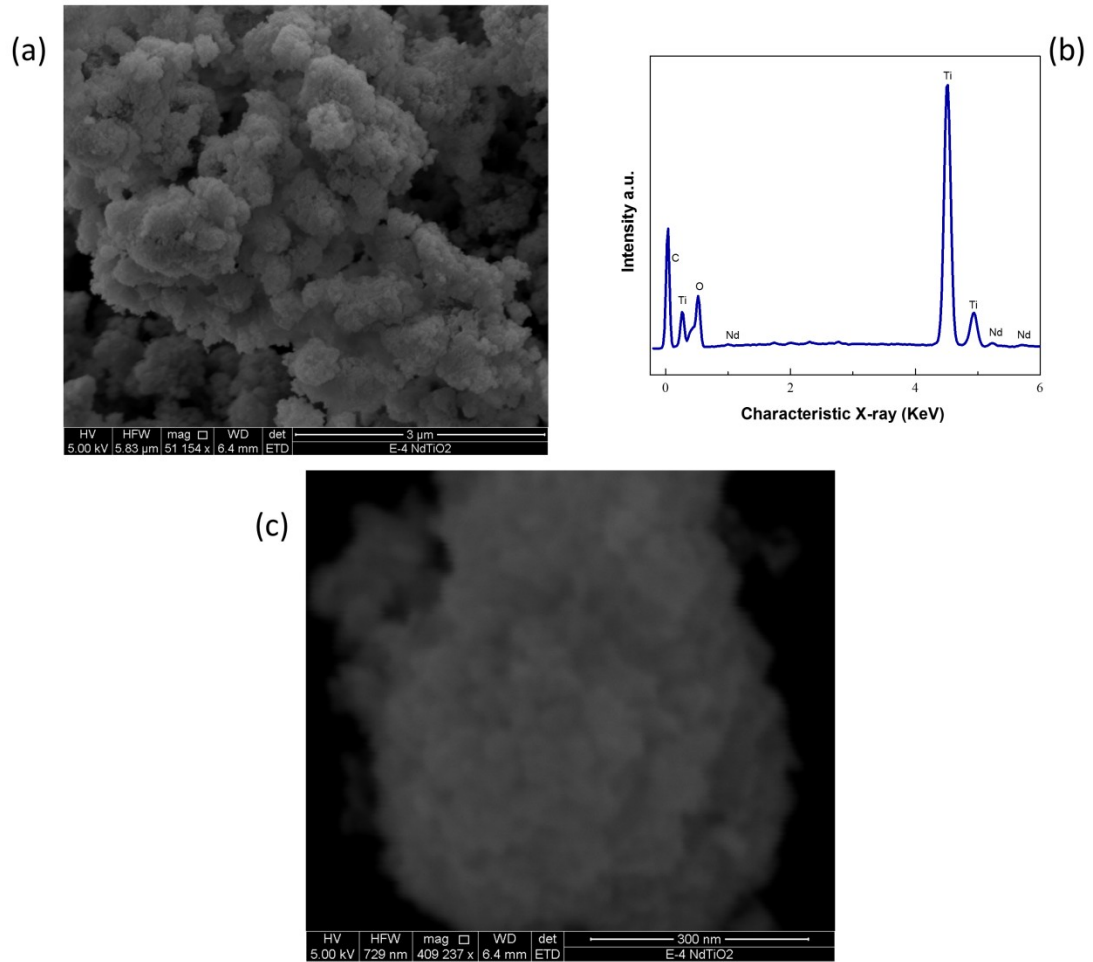
Figure 16. SEM image (Magnification: 51000, at 5KV) (a); EDX data collected from the sample (b); SEM image (Magnification: 400000, at 5KV) (c) of Nd-TiO2 sample

TiO_2 and Ln-TiO_2 nanoparticles. EDX data measured from the Ln-TiO_2 NP samples show

that the amount of the dopant is not more than 2 atomic percent. In order to preserve the

anatase structure of the TiO_2 NPs, it was necessary to keep the amount of dopant low as

the lanthanides have considerably larger ionic radii than the titanium ion. The highly

crystalline nature of the anatase TiO_2 is observable in the TEM images. The majority of

the Ln-TiO_2 nanoparticles are in polyhedral shaped morphologies with higher

concentration of aggregates. The aggregates seen in the micrographs are composed of

fine primary particles.
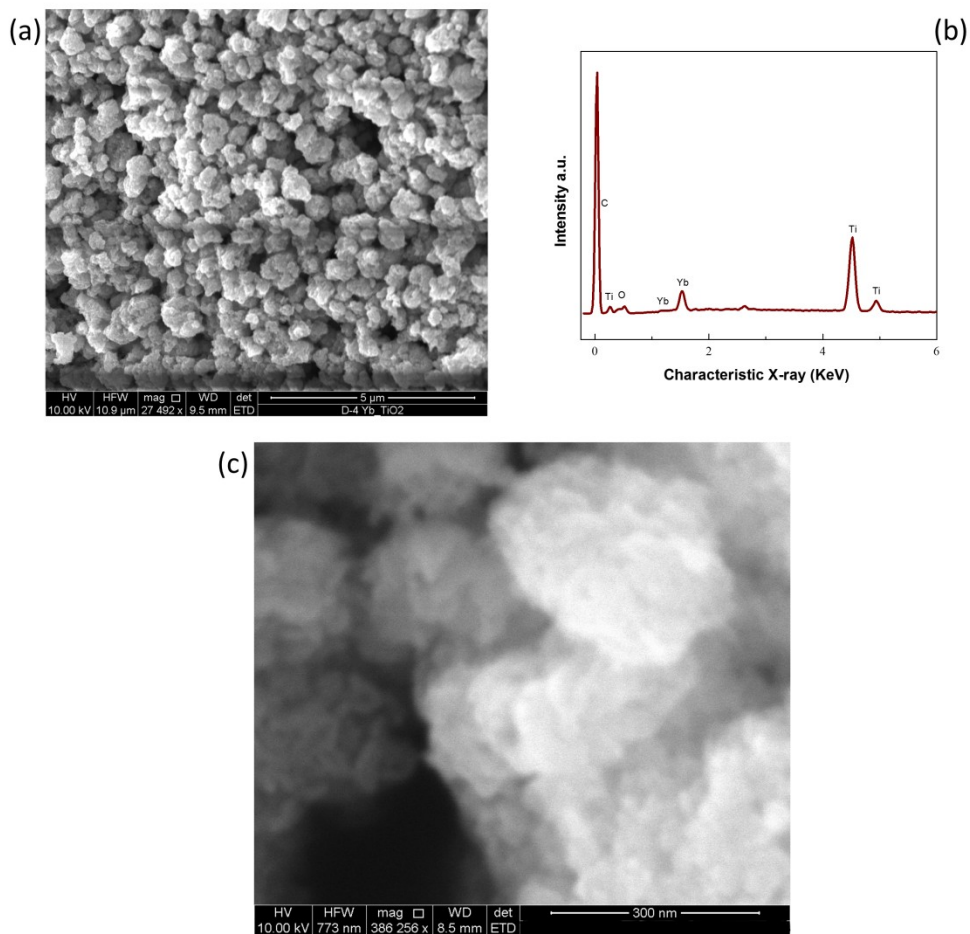
Figure 17. SEM image (Magnification: 27500, at 10KV) (a); EDX data collected from the sample (b), SEM image (Magnification: 400000, at 10KV) (c) of Yb-TiO_2 sample.

4.4 Photoluminescence Spectroscopy (PL):

Photoluminescence spectroscopy (PL) was used as the primary method to gage the samples' potential photocatalytic and gas sensing behavior. An increase in photoluminescence was observed for the Ln- TiO_2 NPs when measurements were made in forming gas at 520°C. In contrast, the measurements at room temperature did not show any noticeable difference in the PL features either in forming
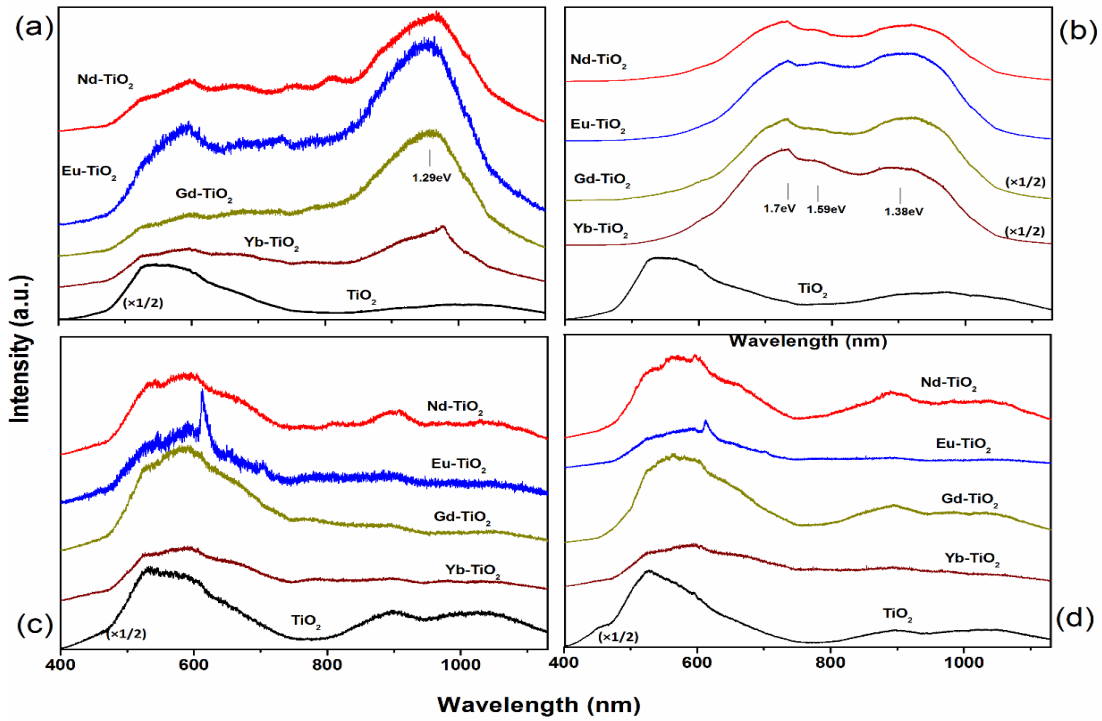
Figure 18. Photoluminescence spectra of the Ln-TiO_2 NP samples: at 520°C in air (a); at 520°C in forming gas (b); at room temperature in air (c); and at room temperature in forming gas (d).

gas or in air environment, but the intensity of PL in forming gas was at least 6 times more than that in air. The defect distribution within anatase TiO_2 structure is a reversible

process with respect to the temperature. The PL measurements at room temperature show that there is no difference in defect distribution before heating and after heating.

The defect states giving rise to PL in the range of 400 to 700 nm are due to oxygen vacancies. The PL features in the near IR defects are due to trapped electron.[22,23] The elimination of an oxygen atom leads to defects such as Ti^{3+} centers and F^+ and F centers where one or two electrons, respectively, are trapped at the vacancies.[24] Near infra-red photoluminescence is enhanced at higher temperatures. The PL shows much reduced peaks at room temperature in IR range. It indicates the trap electrons are obtained by higher temperature in hydrothermally treated Ln-doped samples. The doped samples in forming gas at 520°C shows intense peaks around 1.7 eV, 1.59 eV and 1.38 eV which are attributed to the trapped electrons (fig. 18(b)). The electrons become trapped in levels between the valence band and conduction band of the anatase TiO_2. The trapped electrons go to the valence band, if they release energy, and then recombine with the holes there. These trapped electrons are attributed to the adsorption of the H_2 on the surface of NPs at higher temperature leading to "enhancement of electron trap" defects. The recombination process creates emission of photo-energy which is observed in the PL spectra. At higher temperature the excited electrons undergo diffusion and get trapped at the energetically favorable sites.

The PL measurement made in air show that the intensity of features attributed to oxygen vacancies are higher in the undoped sample than the Ln-doped samples regardless of the measurement temperature (Figure-18 (a), 18(c)). However, for measurements made

in air at 520°C, the PL features due to electron traps are significantly more intense in the Ln-doped sample than the undoped sample. The doped samples contain the Ln ions which can share the f level electrons. The f level electron can mitigate the charge imbalance due to the defects.

As was noted by our group previously in the case of Eu-TiO$_2$ NPs[7], the primary PL peak measured from the Ln-TiO$_2$ NPs is red shifted by approximately 50 nm compared to that of TiO$_2$ NPs. As in the case of Eu-TiO$_2$ NPs reported on previously[7],

Figure 19. Fitted PL curve at 520°C in forming gas for: (a) Nd-doped TiO$_2$, (b) Eu-doped TiO$_2$,(c) Gd-doped TiO$_2$ and (d) Yb-doped TiO$_2$ NP samples.

Table 3. Fitted PL data for the Ln-TiO$_2$ NP samples in forming gas at 520°C

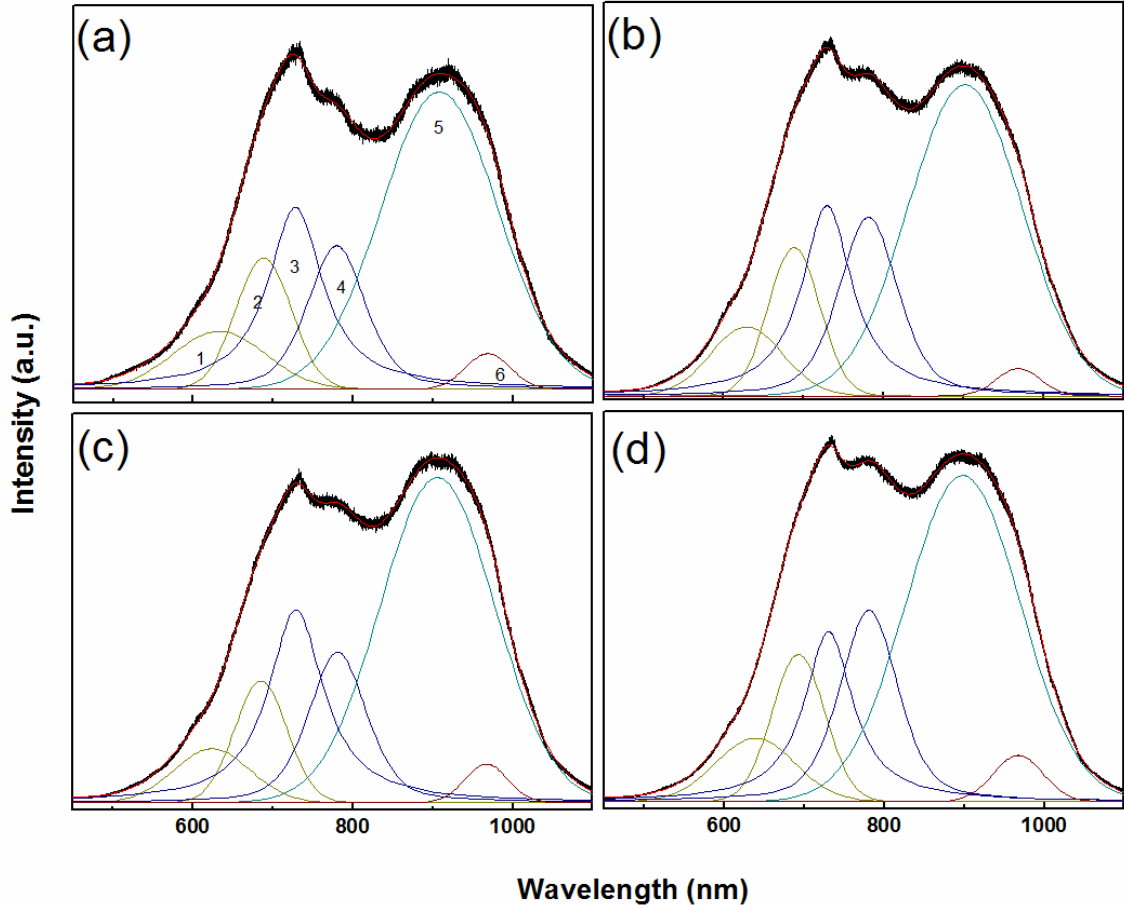| Peak 1	Center (nm)	Area (%)	FWHM (nm)	Shape Factor
Nd-TiO$_2$	632(2)	7.3	135(2)	0
Eu-TiO$_2$	629(1)	6.7	107.1(9)	0
Gd-TiO$_2$	624(1)	5.5	112(1)	0
Yb-TiO$_2$	638(2)	6.5	117(1)	0
Peak 2	Center (nm)	Area (%)	FWHM (nm)	Shape Factor
Nd-TiO$_2$	688.2(4)	10	82.0(9)	0
Eu-TiO$_2$	688.1(3)	10	76.1(8)	0
Gd-TiO$_2$	685.0(3)	8.6	77.5(9)	0
Yb-TiO$_2$	692.5(3)	10	78.2(8)	0
Peak 3	Center (nm)	Area (%)	FWHM (nm)	Shape Factor
Nd-TiO$_2$	727.9(3)	19	82.6(9)	1
Eu-TiO$_2$	729.5(2)	18	75.9(5)	1
Gd-TiO$_2$	728.9(3)	20	83.8(6)	1
Yb-TiO$_2$	730.3(2)	15	73.5(5)	1
Peak 4	Center (nm)	Area (%)	FWHM (nm)	Shape Factor
Nd-TiO$_2$	779.5(4)	13	85(1)	.5
Eu-TiO$_2$	781.1(3)	16	87(1)	.5
Gd-TiO$_2$	781.2(3)	14	86(1)	.5
Yb-TiO$_2$	780.8(3)	17	86(1)	.5
Peak 5	Center (nm)	Area (%)	FWHM (nm)	Shape Factor
Nd-TiO$_2$	908.2(3)	48	172.7(4)	0
Eu-TiO$_2$	902.1(3)	47	168.1(4)	0
Gd-TiO$_2$	905.8(3)	50	168.8(4)	0
Yb-TiO$_2$	898.3(4)	49	169.1(4)	0
Peak 6	Center (nm)	Area (%)	FWHM (nm)	Shape Factor
Nd-TiO$_2$	968.6(4)	2.2	66.0(9)	0
Eu-TiO$_2$	968.4(4)	1.6	64(1)	0
Gd-TiO$_2$	967.2(2)	2.2	63.3(8)	0
Yb-TiO$_2$	967.4(3)	3.0	73.2(8)	0
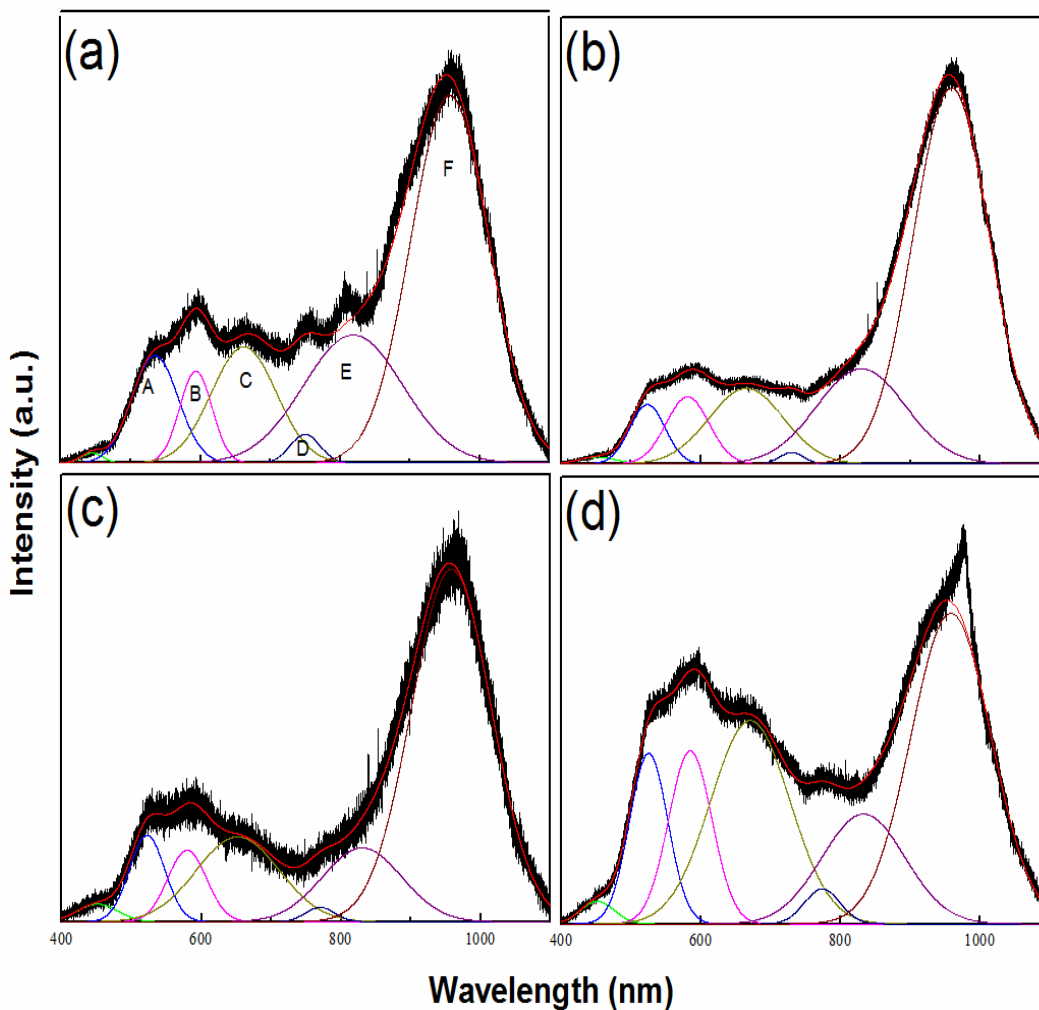
Figure 20. Fitted PL curves at 520°C in air for: (a) Nd-doped TiO_2, (b) Eu-doped TiO_2, (c) Gd-doped TiO_2 and (d) Yb-doped TiO_2 NP samples.

We note the presence of sharp resonance features in the PL associated with f-f transitions of Ln atomic-like states. These features are only observed for Eu- and rather weakly for Nd-doped NPs and stem from energy transfer from self-trapped excitons to Ln ions incorporated in the shell of Ln-TiO_2 NPs. The feature occurring near 590 nm in Eu-doped TiO_2 NPs is attributed to the $^5D_0 \rightarrow {}^7F_1$ transition whereas the feature near 605 and 614

Table 4. Fitted PL data for all the samples in air at 520°C

Peak A	Center (nm)	Area (%)	FWHM (nm)	Shape Factor
Nd-TiO$_2$	535(2)	8.6	78(5)	0
Eu-TiO$_2$	523(1)	4.4	60(4)	0
Gd-TiO$_2$	522(3)	6.4	60(3)	0
Yb-TiO$_2$	525(2)	9.9	64(7)	0
Peak B	Center (nm)	Area (%)	FWHM (nm)	Shape Factor
Nd-TiO$_2$	593(3)	5.13	54(3)	0
Eu-TiO$_2$	581(2)	5.96	72(5)	0
Gd-TiO$_2$	579(1)	5.8	65(3)	0
Yb-TiO$_2$	584(3)	11.4	73(5)	0
Peak C	Center (nm)	Area (%)	FWHM (nm)	Shape Factor
Nd-TiO$_2$	662(1)	13	107(2)	0
Eu-TiO$_2$	665(4)	11.7	126(4)	0
Gd-TiO$_2$	653(3)	14.7	140(5)	0
Yb-TiO$_2$	670(3)	24	133(7)	0
Peak D	Center (nm)	Area (%)	FWHM (nm)	Shape Factor
Nd-TiO$_2$	730(3)	1	40(2)	0
Eu-TiO$_2$	770(2)	1	50(4)	0
Gd-TiO$_2$	774(4)	1.8	60(2)	0
Yb-TiO$_2$	750(3)	2.44	50(3)	0
Peak E	Center (nm)	Area (%)	FWHM (nm)	Shape Factor
Nd-TiO$_2$	818(2)	21	167(5)	0
Eu-TiO$_2$	829(3)	17.5	150(5)	0
Gd-TiO$_2$	830(3)	12.3	134(7)	0
Yb-TiO$_2$	833(4)	14	140(4)	0
Peak F	Center (nm)	Area (%)	FWHM (nm)	Shape Factor
Nd-TiO$_2$	957(2)	50	131(3)	0
Eu-TiO$_2$	958(3)	46.4	129(6)	0
Gd-TiO$_2$	958(2)	58	134(4)	0
Yb-TiO$_2$	958(3)	37.4	134(3)	0

nm is attributed to the $^5D_0 \to {}^7F_2$ f-f transition, for Nd- and Eu-doped TiO_2 NPs, respectively. Interestingly, exposure to forming gas at room temperature is found to stimulate and somewhat reduce the intensity of the $^5D_0 \to {}^7F_2$ f-f transition feature in the Nd- and Eu-doped TiO_2 NP samples, respectively.

Figure 19 shows the fitted PL graphs for all the doped samples in forming gas. Figure 20 shows the fitted PL graphs for all the doped samples in air. The fitted data shown in Tables 3 and 4 clearly indicate the position of the defect peaks in forming gas and air, respectively.

4.5 XPS:

The survey scan shows the presence of dopants and the principle Ti and O peaks (Figure 21). The quantification of the XPS data indicate that the amount of dopants is not more than 2 atomic percent. The XPS quantification agrees with the EDX quantification.

The high resolution XPS analyses (Figure 22) were performed at various ranges according to the survey scans of the individual samples. The XPS of the Nd-TiO_2 NP sample shows peaks at 984 eV and 1007 eV which are due to the Nd $3d_{5/2}$ and Nd $3d_{3/2}$ photoemissions, respectively (Figure 22(a)). The other peaks are due to Auger electron excitations, initiated by the creation of a core hole - this is typically carried out by exposing the sample to a beam of high energy electrons. The XPS of the Eu-TiO_2 NP sample shows peaks at 1135 eV and 1165 eV which are due to the Eu $3d_{5/2}$ and Eu
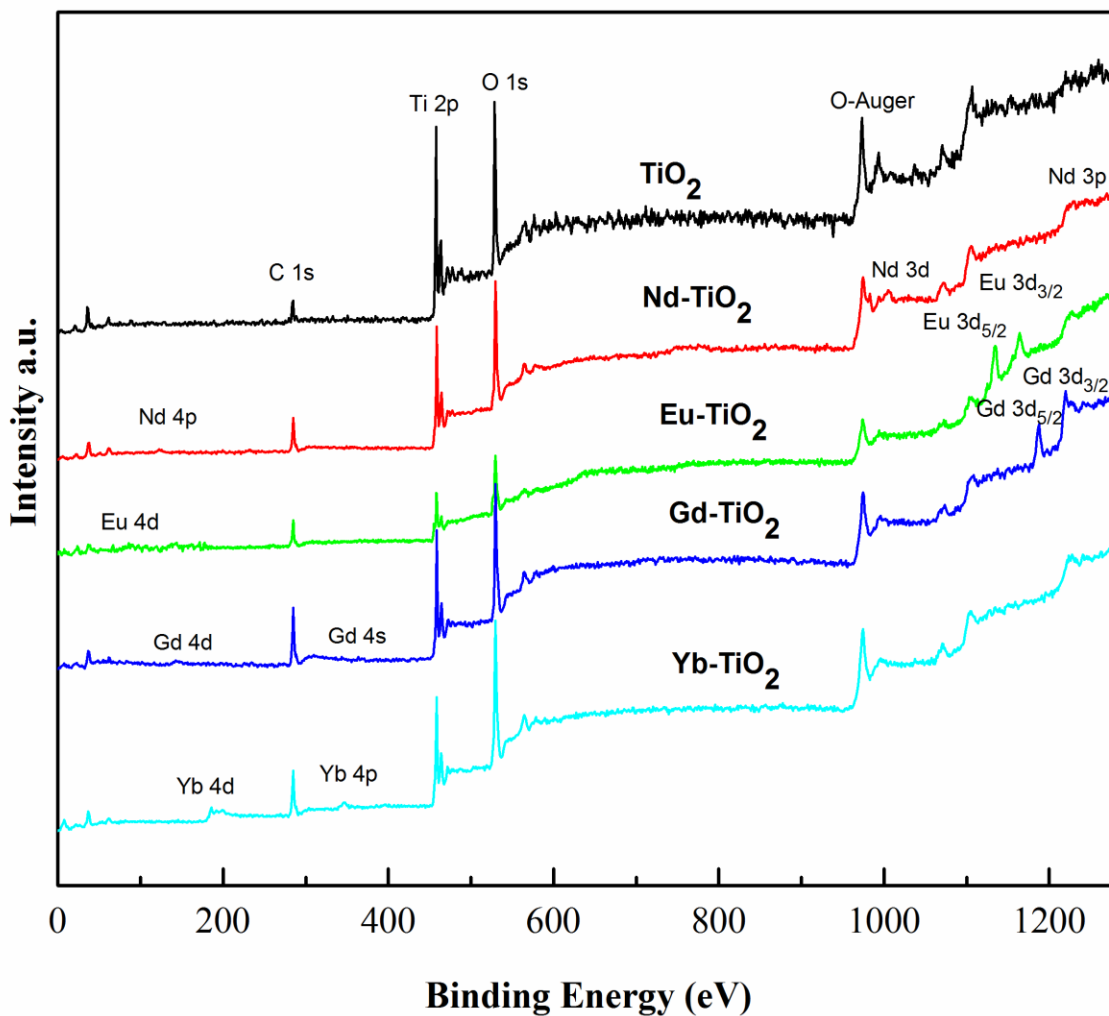
Figure 21. XPS survey scan for the Ln-TiO$_2$ NP samples.

3d$_{3/2}$ photoemissions, respectively (Figure 22(b)). The XPS of the Gd-TiO$_2$ NP sample shows a peak at 144 eV which is due to the Gd 4d photoemission (Figure 22(c)). The XPS of the Yb-TiO$_2$ NP sample shows a peak at 187 eV which is due to the Yb 4d photoemission (Figure 22(d)).
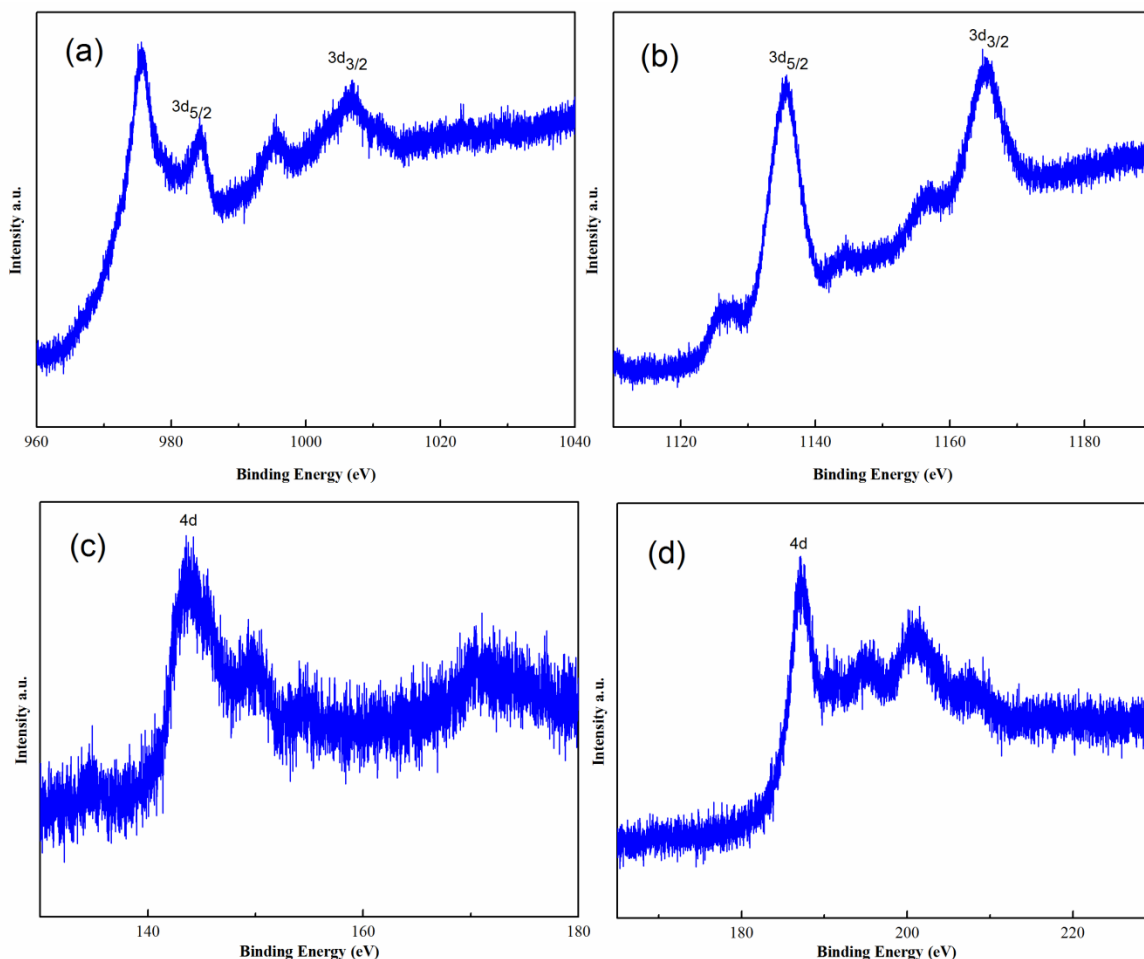
Figure 22. High resolution XPS of Nd in Nd-doped TiO_2 (a); Eu in Eu-doped TiO_2 (b); Gd in Gd-doped TiO_2 (c) and Yb in Yb-doped TiO_2 NP samples (d).

The most noteworthy observations from the XPS analyses are presented in Figures 23 and 24. In Figure 23 (a), the O 1s peak for undoped TiO_2 shows Ti-O bonding and hydroxide type bonding at 531.3 eV and 533 eV respectively. The TiO_2-$Ln_xTi_{(1-x)}O_2$ core-shell NPs exhibit additional bonding features due to Ln-O bonding. The XPS of the Nd-TiO_2 and Eu-TiO_2 NPs shows the Nd-O bonding peak at 529.6 eV (Figure 23(b)) and Table 5) and the Eu-O bonding peak at 528.3 eV (Figure 23(c) and Table 5), respectively.

Figure 23. High resolution scan in the range of O 1s for undoped TiO_2 NP (a); Nd-doped TiO_2 NP (b); Eu-doped TiO_2 NP (c); Gd-doped TiO_2 NP (d) and Yb-doped TiO_2 NP samples (e).

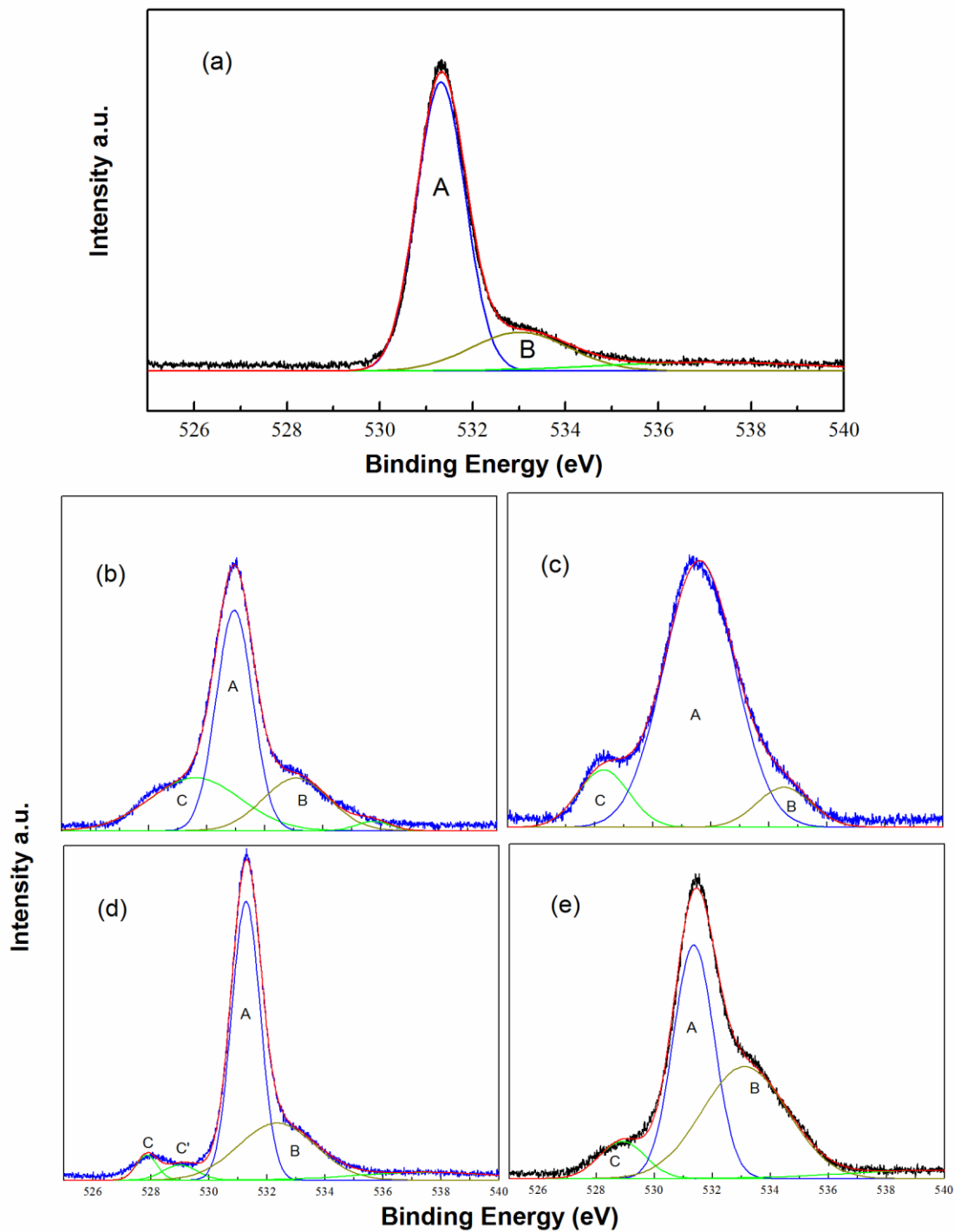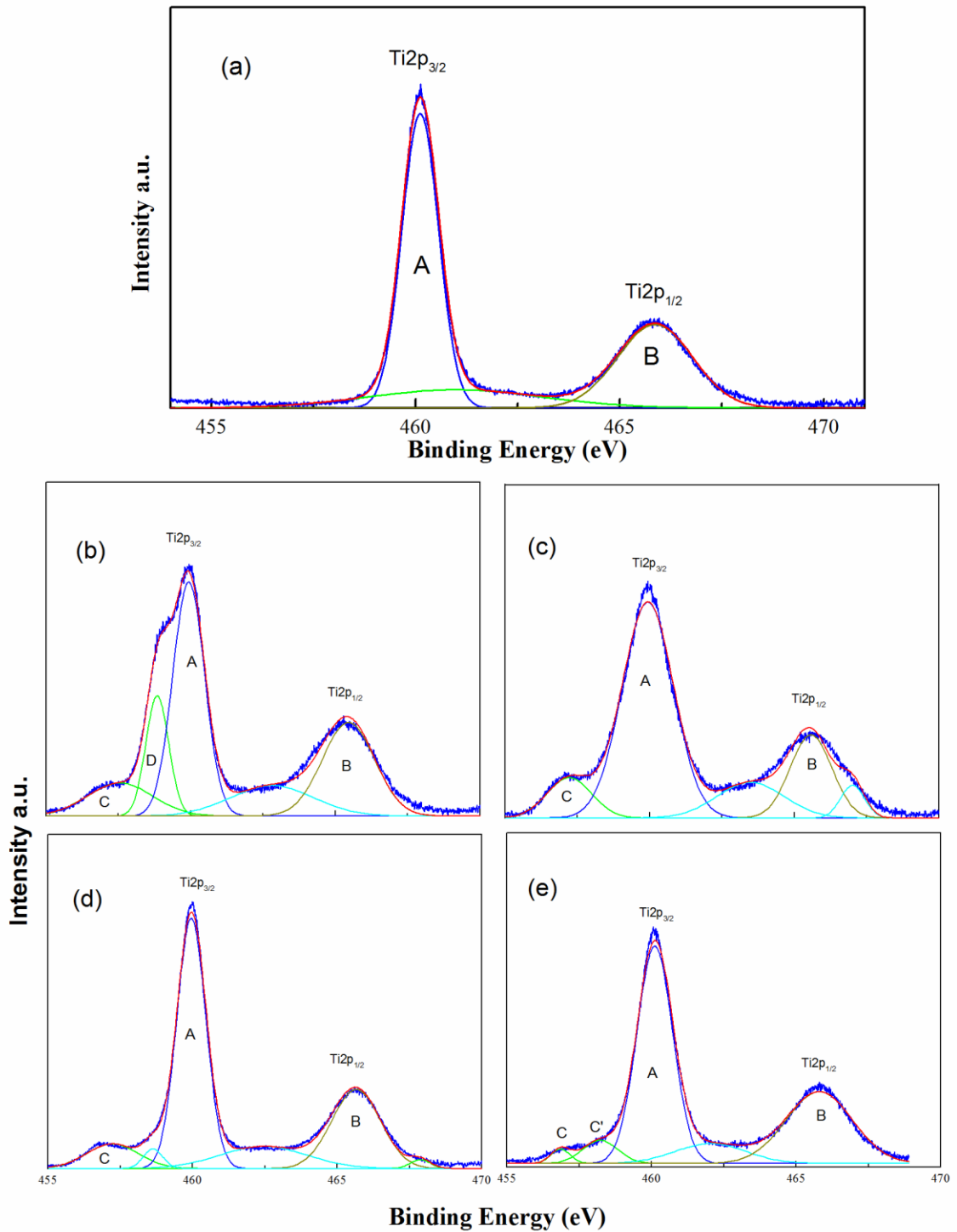Figure 24. High resolution scan in the range of Ti 2p for undoped TiO_2 NP (a); Nd-doped TiO_2 NP (b); Eu-doped TiO_2 NP (c); Gd-doped TiO_2 NP (d) and Yb-doped TiO_2 NP samples (e).

Table 5. High resolution XPS data in the range of O1s (Binding Energy 525-540 eV)

Peak A (Ti-O)	Binding Energy(eV)	Area (%)	FWHM
Undoped TiO_2	531.32	72	1.24
Nd- TiO_2	530.95	49	1.48
Eu- TiO_2	531.60	78	2.88
Gd- TiO_2	531.27	55	1.17
Yb- TiO_2	531.41	52	1.83
Peak B (Hydroxides)	**Binding Energy(eV)**	**Area (%)**	**FWHM**
Undoped TiO_2	533.02	19	2.46
Nd- TiO_2	533.08	21	2.69
Eu- TiO_2	534	9	2.21
Gd- TiO_2	532.34	30	3.13
Yb- TiO_2	533.38	40	3.71
Peak C (Ln-O)	**Binding Energy(eV)**	**Area (%)**	**FWHM**
Nd- TiO_2	529.60	29	3.69
Eu- TiO_2	528.30	12	2.08
Gd- TiO_2 (peak C) (peak C^I)	527.84 529	3.7 3.7	0.84 1.41
Yb- TiO_2	528.78	8	1.78

Table 6. High resolution XPS data in the range of Ti 2P (Binding Energy 455- 470 eV)

Peak A (Ti 2P$_{3/2}$)	Binding Energy(eV)	Area (%)	FWHM
Undoped TiO$_2$	460.10	53	1.06
Nd- TiO$_2$	459.93	38	1.30
Eu- TiO$_2$	459.94	56	2.08
Gd- TiO$_2$	459.96	49	1.18
Yb- TiO$_2$	460.11	52	1.46
Peak B (Ti 2P$_{1/2}$)	Binding Energy(eV)	Area (%)	FWHM
Undoped TiO$_2$	465.87	31	2.17
Nd- TiO$_2$	465.45	25	2.13
Eu- TiO$_2$	465.58	18	1.70
Gd- TiO$_2$	465.65	26	2
Yb- TiO$_2$	465.79	32	2.71
Peak C	Binding Energy(eV)	Area (%)	FWHM
Nd- TiO$_2$	457.56	11	2.68
Eu- TiO$_2$	457.22	10	1.83
Gd- TiO$_2$	457.23	9	2.15
Yb- TiO$_2$(peak C) (peak C^I)	456.85 458.22	2 5	0.8 1.45
Peak D	Binding Energy(eV)	Area (%)	FWHM
Nd- TiO$_2$	458.85	14	1

The XPS of the Gd-TiO$_2$ NPs shows the Gd-O bonding peaks at 527.84 eV and 529 eV (Figure 23(d) and Table 5) whereas the XPS of the Yb-TiO$_2$ NPs shows the Yb-O bonding peak at 528.7 eV (Figure 23(e) and Table 5). In Figure 24(a), we observe two distinct peaks at 460.10 eV and 465.87 eV, which are assigned as the Ti 2P$_{3/2}$ and Ti 2P$_{1/2}$ photoemissions for the undoped TiO$_2$. As can be observed in Table 6, the energy difference between the Ti 2p$_{1/2}$ and Ti 2P$_{3/2}$ peaks is in the 5.7-5.8 eV range, which indicates that the predominance of the 4+ oxidation state of Ti (i.e., Ti^{4+}) in the Ln-TiO$_2$ NP samples.[25] The trend in the energies associated with the Ti 2P$_{3/2}$ peak for all Ln-TiO$_2$ NP samples is consistent with the Ln contraction effect. Also, the binding energy of Ti 2P$_{1/2}$ for the Ln-TiO$_2$ NP samples shows a similar effect. In addition to the Ti 2P$_{3/2}$ and Ti 2P$_{1/2}$ peaks there are some additional peaks in the binding energy range of 456 to 458 eV (Table 6) for all the Ln-doped nanoparticles . These peaks can be explained as being due to the change of local chemical states upon the incorporation of the Ln^{3+} ions within the shell region of the TiO$_2$-Ln$_x$Ti$_{(1-x)}$O$_2$ core-shell NPs. Also, the peaks occurring on the low-energy side of the Ti 2P$_{3/2}$ peak (C and C' in Figure 24) indicate the complete incorporation of the Ln dopants in the anatase Ln$_x$Ti$_{(1-x)}$O$_2$ structure of the shell region of the Ln-TiO$_2$ NPs.[26] We conjecture that peak D in Figure 24(b) is due to sample contamination.

CONCLUSIONS

XRD and Raman measurements confirm the preservation of anatase after hydrothermal treatment. High temperature *in situ* Raman measurements indicate conservation of anatase structure even at 520°C. PL measurements show that the distribution of defect states depends on the environment at high temperature for anatase TiO_2. The hydrothermally treated Ln-TiO_2 NP samples are clearly affected by the surrounding atmosphere (i.e. air or forming gas) by exhibiting substantial modification in the PL under elevated temperature conditions. Measurements show that the PL activation due to surface defect states depends on the type of gas environment (i.e. air or forming gas) at high temperature for hydrothermally treated anatase Ln-TiO_2 NPs. Specifically, exposure to forming gas (5% H_2 and 95% Ar) at 520 °C results in the intensification of PL features at ~1.7 eV and 1.59 eV, which is consistent with adsorption of H_2 on the surface of Ln-TiO_2 NPs resulting in an enhancement of electron trap defects. Our results are consistent with recent theoretical calculations predicting the establishment of electron defect states on the surface of TiO_2 NPs with oxygen vacancies.[11] Specifically, exposure to forming gas at high temperatures results in enhanced oxygen vacancies which can be detected by PL ex situ, and, in situ, results in dramatically enhanced PL intensity. XPS results demonstrate the effect of lanthanide incorporation to the anatase TiO_2 structure by showing the variability in local chemical states. By analyses of the O 1s and Ti 2p XPS peaks for undoped TiO_2 NPs and doped Ln-TiO_2 NP samples, it is shown that Ln ions are precipitated onto the TiO_2 nanoparticles causing formation of TiO_2-$Ln_xTi_{(1-x)}O_2$ core-

shell NPs. Our analyses show that the TiO_2-$Ln_xTi_{(1-x)}O_2$ core-shell NPs exhibit properties which are suitable for applications in gas sensing and offer a step toward realization of the practical use of these materials for various applications, including potentially for photocatalysis. Furthermore, our PL experiments show that Ln ions can provide an f-level electron to compensate for the charge imbalance created by the Ln doping and formation of TiO_2-$Ln_xTi_{(1-x)}O_2$ core-shell NPs.

REFERENCES

[1]W. Choi, Catal. Surveys Asia **10**, 16 (2006).

[2]M. Ni, M.K.H. Leung, D.Y.C. Leung, and K. Sumathy, Renew. Sust. Energy Rev. **11**, 401 (2007).

[3]H. Liu, L. Yu, W. Chen, and Y. Li, J. Nanomater. **2012** (2012).

[4]Z. Zhao and Q. Liu, J. Phys. D: Appl. Phys. **41**, 085417 (2008).

[5]J. Shi, J. Chen, Z. Feng, T. Chen, Y. Lian, X. Wang, and C. Li, J. Phys. Chem. **111**, 693 (2007).

[6]J Moellmann et al, J. Phys.: Condens. Matter **24**, 424206 (2012).

[7]P. A. McCart II, *MS thesis*, Missouri State University (August, 2013).

[8]T. Luttrell, S. Halpegamage, J. Tao, A. Kramer, E. Sutter, and M. Batzill, *Scientific Reports* 4 : 4043 | DOI: 10.1038/srep04043 (2014).

[9]H. Gu , Z. Wang and Y. Hu, Sensors **12**, 5517 (2012).

[10]C. W. Jia, E. Q. Xie, J. G. Zhao, Z. W. Sun, and A. H. Peng, J. Appl. Phys.**100**, 023529 (2006).

[11]A. R. Albuquerque, A. Bruix, I. M. G.Santos, J. R. Sambrano, and F. Illas, J. Phys. Chem. C, **118**, 9677 (2014).

[12]Z. Lin, A. Orlov, R. M. Lambert, and M. C. Payne, J. Phys. Chem. B**, 109**, 20948 (2005).

[13]W. L. Suchanek, and R. E. Riman, Adv. Sci. Technol. **45**, 184-193 (2006).

[14]W. Zhou, R. P. Apkarian, Z. L. Wang, and D. Joy, *Fundamentals of Scanning Electron Microscopy*.

[15]H. Ma, K.J. Shieh, and T. X. Qiao, Nature and Science **4**, 3(2006).

[16]Kevex Instruments, Inc., *Energy-Dispersive X-ray Microanalysis*, Copyright 1983, 1988, 1989, 1999 NORAN Instruments.

[17]A. Clearfield, *Principles and Applications of Powder Diffraction,* edited by J. H. Reibenspies and N. Bhuvanesh (Blackwell Publishing Ltd. ISBN: 978-1-405 16222-7,2008).

[18]J. R. Ferraro, K. Nakamoto and C. W. Brown, *Introductory Raman Spectroscopy*, ISBN: 978-0-12-254105-6.

[19]T. H. Gfroerer, *Encyclopedia of Analytical Chemistry*, edited by R.A. Meyers, pp. 9209–9231 Ó John Wiley & Sons Ltd, Chichester, 2000

[20]C.S. Fadley, J. Electron Spectrosc. Relat. Phenom. **32**, 178 (2010).

[21]D.Wang, J. Zhao, B. Chen and C. Zhu, J. Phys. Condens. Matter **20**,085212 (2008).

[22]F. J. Knorr, C. Mercado, and J. L. McHale, J. Phys. Chem. C **112**, 12786 (2008).

[23]C. Mercado, Z. Seeley, A. Bandyopadhyay, S. Bose, J. L. McHale, Appl. Mater. Interfaces **3**, 2281 (2011).

[24]U. Diebold, Surf. Sci. Rep. **48**, 53 (2003).

[25]H. Fengping, W. Shuai, Z. Shuang, F. Yingge, L. Chunxue, W. Chuang, and L. Chun, Bull. Korean Chem. Soc. **35**, 8 (2014).

[26]D. Nassoko, Y,F, Li, J. L. Li, X. Li, and Y. Yu, Int. J Photoenergy **2012**, 716087 (2012).